Advanced Materials
Research and Technology

https://www.techsyncpress.com

A Review of Propane Dehydrogenation Research Based on Density Functional Theory - Part II

Z. Song

Taizhou University
Taizhou, China
E-mail: songzj@tzc.edu.cn

ABSTRACT: This part focuses on DFT studies of non-oxidative, oxidative, and CO2-assisted dehydrogenation mechanisms, selectivity control, anti-coking behavior, active-site identification, and multiscale modeling approaches.

KEYWORDS: REACTION MECHANISM; SELECTIVITY CONTROL; ANTI-COKING; MICROKINETIC MODELING; MOLECULAR DYNAMICS; MACHINE LEARNING.

3. DFT Studies of Reaction Mechanisms and Selectivity Control

3.1 Non-Oxidative Dehydrogenation Mechanism Research

Non-oxidative propane dehydrogenation (PDH), as the core industrial reaction pathway for propylene production, focuses mechanism research on C-H bond activation pathways, active site-dependent characteristics, and side reaction competition mechanisms. Density functional theory (DFT), with its atomic-scale precision descriptive capabilities, has become the core approach for analyzing PDH reaction essence on different catalyst surfaces. The following systematically summarizes DFT research achievements across various catalyst systems.

3.1.1 PDH Mechanisms on Precious Metal Catalyst Surfaces

Precious metals (Pt, Pd, etc.), due to excellent C-H bond activation capabilities, represent classical PDH catalyst systems. Mechanism research centers on surface facet structures, active site types, and reaction pathway selectivity.

Pt-Based Catalysts: As mainstream industrial PDH systems, Pt-based catalysts exhibit significant facet-dependent surface reaction mechanisms. Through DFT combined with microkinetic analysis, Pt(111) terrace sites follow the traditional reverse Horiuti-Polanyi mechanism, where propane undergoes two consecutive dehydrogenation steps to generate propylene via pathways r1→r4 and r2→r5, with 1-propyl and 2-propyl intermediate formation barriers differing by only 0.02 eV, making both pathways equally favorable. In contrast, low-coordination Pt(211) step sites predominantly follow non-reverse Horiuti-

Polanyi mechanisms (contributing over 50% propylene yield), involving three dehydrogenation steps (removing two β-H and one α-H) plus CH_3CCH_2 hydrogenation, with propylene formation and deep dehydrogenation side reactions forming parallel competitive relationships.[16]

DFT studies further confirm that Pt cluster size influences reaction mechanisms by controlling surface facet ratios: small Pt clusters (predominantly Pt(211)) exhibit lower C-H bond activation barriers with the first dehydrogenation as the rate-controlling step; large Pt clusters (predominantly Pt(111)) show weakened propylene adsorption strength, with the second dehydrogenation becoming the kinetic key step and significantly elevated C-C bond cleavage barriers, enhancing propylene selectivity to 95.8 %.[19]

Pd-Based Catalysts: PDH mechanism research on Pd-based catalysts reveals differences in surface species-assisted dehydrogenation pathways. DFT calculations demonstrate that on Pd(111) and Pd(211) surfaces, direct dehydrogenation and OH-assisted dehydrogenation pathways both outperform O-assisted pathways, with Pd surface dehydrogenation barriers (Pd(111): 1.10 eV; Pd(211): 0.96 eV) significantly lower than Pt-based catalysts (>2.0 eV). Pd surface PDH similarly undergoes two-step dehydrogenation with both 1-propyl and 2-propyl as key intermediates. The OH-assisted pathway in the second dehydrogenation exhibits the lowest barriers, while transition state and final state energies follow scaling relationships similar to methane activation, providing theoretical basis for Pd-based catalyst performance regulation.[62]

3.1.2 PDH Mechanisms on Non-Precious Metal Catalyst Surfaces

Non-precious metals (Ni, Ga-based, etc.), due to cost advantages, have become PDH catalyst research hotspots. Mechanism research emphasizes active site nature, dehydrogenation pathway thermodynamics, and side reaction suppression mechanisms.

Ni-Based Catalysts: Ni-based catalyst PDH mechanisms feature core contradictions between high activity and low selectivity. DFT calculations reveal that on Ni(111) surfaces, propane exhibits physical adsorption (adsorption energy -0.61 eV) while propylene shows chemical adsorption (adsorption energy -1.39 eV), causing propylene to readily undergo deep dehydrogenation rather than desorption. Two PDH pathways exist: 1-propyl pathway (first dehydrogenation barrier 0.69 eV) and 2-propyl pathway (first dehydrogenation barrier 0.79 eV), with the 1-propyl pathway kinetically and thermodynamically more favorable, exhibiting two-step dehydrogenation barriers (0.69 eV and 0.09 eV) both lower than Pt(111) surfaces.

However, Ni(111) surface C-C bond cleavage barriers (minimum 1.14 eV) approach propylene desorption barriers (1.16 eV), with deep dehydrogenation barriers (0.84-0.85 eV) lower still, causing side reactions to dominate and poor propylene selectivity—consistent with experimental observations of Ni-based catalyst coking deactivation.

Ga-Based Catalysts: Ga-based catalyst PDH mechanisms closely relate to Ga species existence forms, with different supports and preparation conditions causing significant active site variations.[63] Through DFT combined with experimental characterization, extra-framework Ga^+ in CHA zeolites serves as the PDH active center, reacting with H_2 to generate GaH_x (formation enthalpy -51.2 $kJ \cdot mol^{-1}$). The mechanism involves propane C-H bond oxidative addition cleavage forming $[HGa(III)-C_3H_7]^+$ intermediates, followed by β-H elimination generating propylene. Ga^+ transition state stabilization makes its dehydrogenation rate 43 times that of In^+ sites.[42]

DFT studies of $Ga_2O_3(100)$ surfaces reveal bicoordinate oxygen sites O(2) as primary active centers for initial C-H bond activation, following radical mechanisms (barrier 18.1 kcal/mol). Subsequent propylene can be generated through second-step dehydrogenation of propyl radicals, propoxy, or propyl-gallium intermediates, with rate-controlling steps transitioning from O(2) site dehydrogenation to Ga site dehydrogenation forming GaH species as reactions progress.

3.1.3 Common Patterns in Reaction Mechanisms and Regulatory Insights

Synthesizing DFT research results across different catalyst systems, non-oxidative PDH reaction mechanisms exhibit the following common features:

First, reactions all undergo two consecutive dehydrogenation steps, with 1-propyl and 2-propyl as universally present key intermediates, where first-step C-H bond activation often constitutes the rate-controlling step (Pt(211), Ni(111), Ga_2O_3, and other systems).

Second, catalyst surface active site coordination environments determine reaction pathways. Low-coordination sites (steps, edge sites) typically possess lower dehydrogenation barriers but readily trigger deep dehydrogenation, while high-coordination sites (terrace sites) show slightly lower activity but higher propylene selectivity.

Third, the relative magnitude of propylene desorption barriers versus deep dehydrogenation barriers represents the core factor determining selectivity. Reducing propylene adsorption strength and increasing deep dehydrogenation barriers constitute key directions for selectivity control.

DFT research provides clear insights for mechanism-guided PDH catalyst design: for precious metal catalysts, particle size regulation can optimize facet ratios, or alloying elements can regulate active site coordination environments; for non-precious metal catalysts, support modification can stabilize specific active species (such as Ga^+), or spatially confined structures can suppress propylene deep dehydrogenation and C-C bond cleavage. These strategies have all been thermodynamically and kinetically validated in DFT studies.

3.2 Oxidative Dehydrogenation (ODHP) Mechanism Studies

Oxidative dehydrogenation of propane (ODHP) has emerged as an important alternative route for propane-to-propylene conversion, leveraging thermodynamic advantages and anti-coking characteristics. The mechanistic core focuses on the action mechanisms of active oxygen species, C-H bond activation pathways, and strategies to suppress deep oxidation. Density functional theory (DFT) provides critical support for revealing the essential nature of ODHP reactions in different systems through atomic-scale analysis of catalyst surface species evolution and electron transfer patterns. The following presents a systematic summary based on DFT research achievements for typical catalyst systems including vanadium-based, boron-based, and carbon-nitrogen-based catalysts.

3.2.1 ODHP Mechanisms on Vanadium-Based Catalyst Surfaces

Vanadium-based catalysts (V_2O_5, VO_x/CeO_2, etc.) represent the most extensively studied ODHP systems, with mechanistic cores centered on surface oxygen species types, C-H bond activation pathways, and selectivity control mechanisms. The ODHP mechanism on V_2O_5 surfaces exhibits significant active site dependence. DFT calculations reveal that vanadyl (V=O) sites on the V_2O_5(010) surface serve as the core for initial C-H bond activation. Propane undergoes dissociative adsorption to form isopropoxy and hydroxyl species, where the activation energy for isopropoxy formation (9.4 kcal/mol) is significantly lower than that for n-propoxy (14.5 kcal/mol), making it more favorable both thermodynamically and kinetically. The second dehydrogenation step requires hydroxyl species on three-coordinate bridging oxygen (O(3)) sites, releasing propylene and water through a cooperative process with an activation energy of approximately 15 kcal/mol.

Further studies confirm that the V_2O_5(001) surface contains two types of active oxygen sites: terminal oxygen (O(1)) and bridging oxygen (O(2)). Terminal oxygen can activate C-H bonds through both radical mechanisms and oxygen insertion mechanisms, while bridging oxygen can only react via oxygen insertion mechanisms. Moreover, isopropoxy exhibits lower desorption energy at bridging oxygen sites (6.2 kcal/mol), resulting in higher propylene selectivity.

The ODHP mechanism on supported VO_x/CeO_2 catalysts highlights the synergistic effects between support and active components. DFT combined with electronic structure analysis demonstrates that the

$VO_3/CeO_2(111)$ surface possesses unique "new empty localized states (NELS)", which are primarily composed of O 2p orbitals from VO_3 species and can efficiently capture electrons to assist in breaking the first C-H bond of propane with an activation energy of only 0.12 eV [Fig. 7(c)-(e)].

However, breaking the second C-H bond requires an activation energy as high as 1.81 eV, because NELS becomes occupied after the first dehydrogenation step, and subsequent dehydrogenation must rely on Ce 4f orbitals. The repulsion between localized electrons significantly increases the energy barrier, thereby suppressing deep oxidation.

The deep oxidation mechanism of vanadium-based catalysts has been clearly elucidated. [36] Through systematic DFT exploration of deep oxidation pathways on the $V_2O_5(001)$ surface, terminal oxygen (O(1)) was found to be the primary site for side reactions. Isopropoxy can be converted to acetone at this site, which is further oxidized to acetic acid and formaldehyde, ultimately decomposing to CO_x. In contrast, bridging oxygen (O(2)), while capable of activating C-H bonds, shows no activity toward acetone formation and deep oxidation, making it a high-selectivity site [Fig. 7(a)]. This research also revealed the reactivity order of hydrocarbons: acetic acid ≈ acetone < propane < acrylic acid < propylene < acrolein, which aligns with C-H bond strength patterns and provides theoretical basis for selectivity control. [35]

3.2.2 ODHP Mechanisms on Boron-Based Catalyst Surfaces

Boron-based catalysts (h-BN, B_2O_3, etc.), as representatives of metal-free catalytic systems, have ODHP mechanisms centered on the formation of surface oxygen-containing boron species, C-H bond activation modes, and deep oxidation suppression mechanisms. Peroxo species on boron-based catalyst surfaces are key active centers for ODHP. DFT calculations confirm that >B-O-B< sites at the zigzag edges of h-BN can in-situ generate boron peroxo species (>B-O-O·, >B-O-OH, etc.) during reactions. These species possess highly selective activation capability for secondary C-H bonds of propane [Fig. 7], with a dehydrogenation activation energy of only 13.5 kcal/mol and isopropyl selectivity ($CH_3\dot{C}HCH_3/\cdot CH_2CH_2CH_3$) reaching 34.95, far exceeding that of simple >B-O· sites (2.22).[50] Isopropyl readily undergoes β-H elimination to produce propylene, while n-propyl tends to undergo C-C bond cleavage initiating deep oxidation—this characteristic is the core reason for the high selectivity of boron-based catalysts.

The synergistic effects of detached nano-B_2O_3 clusters further refine the boron-based catalytic mechanism. Nano-B_2O_3 clusters detached from the catalyst surface can capture gas-phase propoxy radicals ($\cdot OC_3H_7$) through substitution reactions with an energy barrier of approximately 24 kcal/mol, thereby suppressing deep oxidation product formation. Internal three-coordinate boron sites (B_i) within these clusters, due to fewer hydroxyl substitutions and stronger oxophilicity, exhibit significantly higher radical capture activity than edge sites (B_t, B_m), providing new directions for catalyst design.

The synergistic mechanism between gas-phase and surface reactions is indispensable in boron-based catalysis. [57] Simulations using deep potential models trained by DFT reveal that ODHP on boron-based catalysts follows a hierarchical reaction network of "surface initiation - gas-phase propagation": surface sites initiate propane C-C bond cleavage to generate methyl and ethyl radicals, followed by O_2 abstracting hydrogen to produce ·OOH, which decomposes to ·OH to accelerate propane dehydrogenation. N-propyl radicals can isomerize to isopropyl (exothermic by 2.84 kcal/mol) and then dehydrogenate to form propylene [Fig. 7(b)].

At high temperatures, C-C bond cleavage of n-propyl is the primary pathway for ethylene formation, while low-temperature conditions favor isomerization reactions, enhancing propylene selectivity.[15]

3.2.3 ODHP Mechanisms on Carbon-Nitrogen-Based and Other Catalyst Surfaces

The ODHP mechanisms of carbon-nitrogen-based (C_3N, g-C_3N_4) and multi-component metal oxide (Mo-V-Te-Nb-O) novel catalysts reveal unique advantages and control principles of non-vanadium-based systems. The ODHP mechanism of C_3N materials centers on radical pathways and defect site regulation. DFT combined with microkinetic simulations demonstrate that C-O functional groups on the C_3N surface

are active centers for C-H bond activation. ODHP follows a radical mechanism, with the first C-H bond breaking as the rate-controlling step (activation energy 0.78-1.44 eV).[64] N vacancies and edge sites are critical for selectivity control—at 775 K with 13% propane conversion, these sites achieve 65.1% propylene selectivity, while C-O sites on perfect surfaces show 0% selectivity. During catalyst regeneration, hydroxyl coupling ($2OH^* \rightarrow H_2O^* + O^*$) competes with O_2-involved oxidation pathways ($2OH^* + O_2^* \rightarrow H_2O_2^* + 2O^*$), with low oxygen partial pressure favoring suppression of deep oxidation.

The ODHP mechanism of Mo-V-Te-Nb-O M1 phase catalysts reflects synergistic effects of multi-component metals. DFT calculations reveal that the active center consists of V^{5+}=O, Te^{4+}=O, and Mo^{6+} sites. Initial propane dehydrogenation occurs at V^{5+}=O sites with an activation energy of 1.74 eV as the rate-controlling step. The second dehydrogenation is completed by Te^{4+}=O sites with significantly reduced activation energy, and isopropyl conversion to propylene is exothermic by 1.73 eV. Mo=O sites only participate as hydrogen acceptors without directly activating propane, maintaining the catalyst redox cycle.[65]

3.2.4 Common Principles and Control Insights for ODHP Mechanisms

Integrating DFT research results from different catalyst systems, ODHP reaction mechanisms exhibit the following common characteristics: First, initial C-H bond activation is the rate-controlling step, with the type of active oxygen species (terminal oxygen, bridging oxygen, peroxo species, etc.) determining the activation pathway (radical mechanism, oxygen insertion mechanism, etc.), and isopropoxy being a universally present key intermediate. Second, selectivity is determined by the relative magnitude of intermediate desorption energy and deep oxidation energy barriers—weakly adsorbed intermediates readily desorb to form propylene, while strongly adsorbed intermediates tend to undergo deep oxidation or C-C bond cleavage. Third, catalyst surface defects (vacancies, edge sites) and support-active component synergistic effects can modulate the reactivity of active oxygen species to achieve selectivity optimization.

DFT research provides clear insights for mechanism-guided design of ODHP catalysts: For vanadium-based catalysts, surface oxygen species ratios can be modulated (increasing bridging oxygen content) or supports can be introduced (such as CeO_2) to form unique electronic structures (NELS) that suppress deep oxidation. For boron-based catalysts, surface peroxo species generation conditions can be optimized or defect sites introduced to enhance selective activation capability for secondary C-H bonds. For carbon-nitrogen-based catalysts, N vacancy density and oxygen partial pressure can be regulated to balance activity and selectivity. These strategies have all been validated thermodynamically and kinetically in DFT studies, providing theoretical support for developing high-efficiency ODHP catalysts.

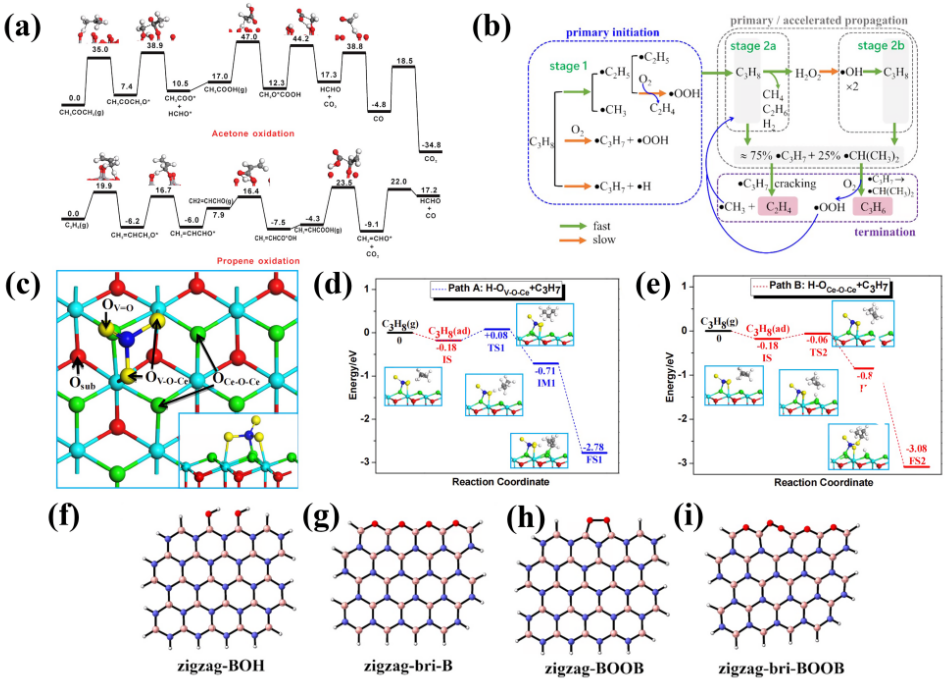

Figure 7. (a)Lowest energy profiles of deep oxidations of acetone and propene. (b) Hierarchical reaction network. (c) Top view of the calculated $VO_3/CeO_2(111)$ catalyst (insert: side view). The balls in dark blue represent V atoms, whereas those in cyan represent Ce atoms. Four different types of O atoms are labelled: the balls in yellow represent two types of oxygen atoms, namely, OV=O and OV-O-Ce, at VO_3, balls in green represent top-surface oxygen atoms OCe-O-Ce on $CeO_2(111)$, and those in red are sub-surface oxygen atoms Osub in $CeO_2(111)$. Calculated two reaction pathways for breaking the first C–H bond in C_3H_8 on VO_3/CeO_2 (111). (d) Path A; (e) Path B. Models used in the study: (f) zigzag-BOH, (g) zigzag-bri-B, (h) zigzag-BOOB, and (i) zigzag-bri-BOOB. Color scheme: B in pink, N in blue, O in red, and H in white

3.3 CO_2-Assisted Dehydrogenation (CO_2-ODHP) Mechanism Studies

CO_2-assisted oxidative dehydrogenation of propane (CO_2-ODHP) has become an important pathway for propane-to-propylene conversion, leveraging CO_2's hydrogen consumption effect, anti-coking characteristics, and carbon resource utilization advantages. DFT research focuses on CO_2 activation mechanisms, synergistic effects between CO_2 and propane dehydrogenation, active site nature, and selectivity control principles, systematically revealing the reaction essence of CO_2-ODHP under different catalyst systems. The following summarizes DFT research achievements for Cr-based, Pt-based, Ga-based, and other multi-component oxide catalysts.

3.3.1 CO_2-ODHP Mechanisms on Cr-Based Catalysts

Cr-based catalysts represent classic systems for CO_2-ODHP, with mechanistic cores centered on Cr active valence evolution, CO_2 activation pathways, and synergistic control of C-H bond activation. Mechanistic studies of $Ce_xZr_{1-x}O_2$-supported CrO_x catalysts clarify active species and reaction pathways. DFT calculations confirm that Cr^{3+} is the core active species for CO_2-ODHP, following a non-redox direct dehydrogenation pathway. The energy barrier for initial propane C-H bond activation to generate isopropyl intermediates is 2.16 eV (on Cr/ZrO_2 surface), significantly lower than the C-C bond cleavage barrier (1.07 eV), thermodynamically favoring dehydrogenation reactions. The second dehydrogenation step to produce

propylene has an energy barrier of only 0.80 eV, while CO_2 activation (generating CO and O*) has a barrier as high as 2.58 eV, indicating that propane dehydrogenation is the fast step and CO_2 conversion is the rate-controlling step. Ce doping modulates the Cr^{3+} electronic environment, expanding the energy barrier difference between C-C bond cleavage and dehydrogenation from 0.27 eV to 0.88 eV, significantly suppressing cracking side reactions and enhancing propylene selectivity.

The mechanism of Cr-ZrO_x solid solution catalysts highlights the role of electron transfer and defect regulation.[66] DFT calculations reveal that Zr introduction causes Cr species to form highly dispersed Cr^{6+} species, whose redox cycle with Cr^{3+} ($Cr^{6+} \rightarrow Cr^{3+} \rightarrow Cr^{6+}$) is key to synergistic CO_2 activation and propane dehydrogenation. CO_2 dissociation at oxygen vacancies to generate O* and CO has an energy barrier of 2.43 eV. O* can capture H* produced from propane dehydrogenation to form OH, promoting H_2 desorption. Bader charge analysis shows that Zr's electronegativity difference reduces Cr atom electron cloud density, strengthening C-H bond polarization and activation, decreasing initial dehydrogenation barrier from 1.2 eV to 0.8 eV.[5]

3.3.2 CO_2-ODHP Mechanisms on Pt-Based Catalysts

The CO_2-ODHP mechanism of Pt-based catalysts centers on metal-oxide interface synergy and competitive adsorption regulation between CO_2 and propane, with selectivity dependent on Pt active site isolation and electronic state control. The mechanism of Pt-M (M=Sn, In, Zn) bimetallic catalysts reveals tandem reaction characteristics. DFT calculations confirm that CO_2-ODHP follows a two-step tandem mechanism of "direct propane dehydrogenation + reverse water-gas shift (RWGS)", with RWGS as the rate-controlling step. The Pt_3Sn-SnO_x interface is the core active site, where Pt^0 low-coordination sites are responsible for propane C-H bond activation (barrier 0.25 eV), and SnO_x sites promote CO_2 adsorption and activation (CO_2 adsorption energy -0.78 eV). In the RWGS reaction, formation of HOCO* intermediate from CO_2 and H* has a barrier of 1.12 eV, significantly higher than the propane dehydrogenation barrier.

Moreover, Pt-Sn alloying increases the C-C bond cleavage barrier from 0.51 eV to 2.21 eV, effectively suppressing cracking side reactions.

The mechanism of Pt_4/Fe-MFI catalysts demonstrates the regulatory role of framework Fe.[67] DFT calculations show that framework Fe stabilizes Pt_4 clusters through geometric anchoring and electronic modulation, enhancing propane adsorption energy from -0.59 eV to -0.92 eV and reducing initial C-H bond activation barrier to 0.51 eV.[68] CO_2 molecules do not directly participate in H* consumption elementary reactions (its barrier with H* exceeds 1.37 eV) but modulates electronic states through adsorption, decreasing propylene desorption energy from 0.62 eV to 0.31 eV while suppressing propylene deep dehydrogenation (barrier increases from 0.91 eV to 1.01 eV), indirectly enhancing catalytic performance.

3.3.3 CO_2-ODHP Mechanisms on Ga-Based Catalysts

The CO_2-ODHP mechanism of Ga-based catalysts features bimetallic synergistic activation and novel intermediate pathways, breaking through traditional RWGS synergistic mechanisms. Ga-Ce bimetallic oxide catalysts propose a new isopropanol intermediate mechanism. DFT combined with in-situ characterization confirms that CO_2 activates at Ce^{3+} sites to generate -COO* intermediates, which dissociate to CO and O* with a barrier of 1.8 eV. O* combines with H on propane β-C to form OH*, which reacts with isopropyl intermediates to generate isopropanol (barrier 0.6 eV). Isopropanol dehydration to form propylene has a barrier of only 0.3 eV, significantly lower than direct dehydrogenation (1.2 eV).[69] The introduction of Ga increases Ce^{3+} content, strengthening CO_2 adsorption energy from -0.4 eV to -0.8 eV while suppressing excessive oxidation activity of O*, achieving 93.46% propylene selectivity.

3.3.4 CO_2-ODHP Mechanisms on Other Catalyst Systems

Beyond classic Cr, Pt, and Ga-based systems, DFT studies of multi-component catalysts such as Co-Zr doped CeO_2 and MgO-modified VO_x@ZrO_2 reveal unique mechanisms of defect regulation and multi-component synergy. The mechanism of Co-Zr co-doped CeO_2 catalysts focuses on oxygen vacancies and

photo-thermal synergy. DFT calculations show that Co and Zr co-doping reduces oxygen vacancy formation energy on CeO_2 surface from 1.08 eV to 0.44 eV, strengthening CO_2 adsorption energy at oxygen vacancies to -0.6 eV. CO_2 activation at oxygen vacancies to generate O* has a barrier of 1.88 eV. O* assists propane C-H bond activation, reducing the barrier from 0.72 eV to 0.44 eV. Simultaneously, hybridization of Co 3d orbitals with Ce 4f orbitals narrows the band gap, promoting photogenerated carrier separation. Photo-thermal synergy reduces overall reaction barriers by 20%, achieving low-temperature high-efficiency catalysis.

The mechanism of MgO-modified $VO_x@ZrO_2$ catalysts demonstrates synergy between acid-base sites and oxygen species. Related DFT studies show that MgO introduction increases medium-strength basic sites on catalyst surfaces, enhancing CO_2 adsorption energy from -0.5 eV to -0.9 eV and reducing activation barrier from 2.3 eV to 1.7 eV.

Simultaneously, MgO-VO_x interactions modulate lattice oxygen activity, decreasing propane C-H bond activation barrier from 1.1 eV to 0.8 eV while suppressing further reactions between propylene and lattice oxygen (barrier increases from 1.5 eV to 2.1 eV), synergistically improving both conversion and selectivity.

3.3.5 Common Principles and Control Insights for CO_2-ODHP Mechanisms

Integrating DFT studies of different catalyst systems, CO_2-ODHP mechanisms exhibit the following common characteristics: First, CO_2 activation pathways are primarily divided into two types—oxygen vacancy-assisted dissociation (generating O* and CO) and RWGS reactions (generating CO and H_2O with H*). The former is common in redox-active catalysts, while the latter is more prevalent in non-redox systems, and CO_2 activation barriers are generally higher than propane dehydrogenation barriers. Second, active sites are typically metal cations (Cr^{3+}, Pt^0, Ga^{3+}, Ce^{3+}) or metal-oxide interface sites, whose electronic states (charge density, d-orbital energy levels) and geometric structures (coordination number, bond length) determine C-H bond activation and CO_2 adsorption capabilities. Third, the core of selectivity control is expanding the difference between "C-H bond activation barrier and C-C bond cleavage/over-oxidation barrier", achievable through metal doping, support modification, and defect engineering.

DFT research provides clear directions for CO_2-ODHP catalyst design: For Cr-based catalysts, Ce, Zr, and other element doping can modulate Cr valence state and electronic environment to strengthen CO_2 activation and dehydrogenation synergy. For Pt-based catalysts, bimetallic interfaces can be formed with Sn, Fe, and other metals to isolate Pt active sites and reduce CO_2 activation barriers. For Ga-based catalysts, bimetallic synergy can construct novel intermediate pathways to reduce reaction barriers and suppress over-oxidation. These strategies have all been validated for thermodynamic and kinetic feasibility through DFT calculations, providing theoretical support for developing high-efficiency CO_2-ODHP catalysts.

3.4 Selectivity Control and Anti-Coking Mechanisms

The selectivity core of propane dehydrogenation (PDH) reactions lies in suppressing side reactions such as propylene deep dehydrogenation and C-C bond cleavage while mitigating catalyst deactivation caused by coke deposition. DFT research, by revealing key factors such as active site structure, electronic state modulation, and intermediate adsorption-desorption equilibrium, clarifies the intrinsic correlation between selectivity control and anti-coking performance, providing precise guidance for catalyst structure optimization. The following systematically summarizes selectivity control principles and anti-coking mechanisms based on DFT research achievements for Pt-based, Ni-based, Ru-based, and Cr-based catalyst systems.

3.4.1 Active Site Geometry and Electronic State Regulation Mechanisms

Geometric isolation of active sites and electronic-state modulation are core strategies for achieving high selectivity. By disrupting continuous metal active sites and tuning the d-band center, these approaches optimize the adsorption strength of reaction intermediates and suppress undesired side reactions.

3.4.1.1 Geometric isolation effect

Geometric isolation, achieved by introducing a second metal or by support modification, disrupts the continuous arrangement of metal atoms and reduces multi-atom active sites, thereby suppressing side reactions that rely on adjacent metal centers. DFT studies on Pt–Cu single-atom alloys (SAAs) confirm that the incorporation of Cu disperses Pt atoms in an isolated form within the Cu matrix, generating isolated Pt active sites. Combined DFT and kinetic Monte Carlo (kMC) simulations reveal that isolated Pt sites weaken propylene adsorption energy from –0.65 eV on Pt(111) to –0.47 eV, while increasing the C–C bond-scission barrier from 1.73 eV to above 2.05 eV, effectively suppressing cracking side reactions. Moreover, the forward rate constant for propylene deep dehydrogenation (3.12×10^{14} s^{-1}) is far lower than the reverse rate constant (1.77×10^{13} s^{-1}), further locking in high propylene selectivity.[9]

The geometric modulation mechanism of Ni–In alloys highlights the role of the "degree-of-isolation" descriptor. DFT calculations show that the Ni–Ni distance in Ni–In alloys (3.177 Å) is significantly larger than that in pure Ni (2.479 Å), and the resulting isolated Ni sites increase the energy barrier for propylene deep dehydrogenation from 0.8 eV to 1.2 eV, while raising the C–C bond-scission barrier to above 2.0 eV. A volcano-type relationship established based on the degree-of-isolation descriptor indicates that a moderate level of Ni atom isolation (0.15–0.20) enables propylene selectivity above 91%, validating the critical role of geometric isolation.[58]

3.4.1.2 Electronic-state modulation effects

Electronic-state modulation regulates the adsorption strength of reaction intermediates by altering the charge density or the d-band center of active metal sites, thereby balancing C–H bond activation with propylene desorption efficiency. The electronic-modulation mechanism of Pt–In single-atom alloys has been clearly established.[1] Lin et al. demonstrated via DFT calculations that electron transfer from In to Pt shifts the Pt d-band center from –2.25 eV to –2.14 eV, weakening propylene adsorption from –1.26 eV to 0.28 eV and reducing the adsorption energy of the 1-propyl intermediate from –4.46 eV to –2.8 eV. These changes accelerate propylene desorption and suppress deep dehydrogenation. Meanwhile, the electron-rich Pt sites exhibit weakened interaction with the π electrons of propylene, resulting in a lower desorption barrier compared to the deep-dehydrogenation barrier (0.31 eV vs 1.01 eV), thereby significantly enhancing selectivity.

The d-band-center modulation mechanism in Pd–In alloys has also been confirmed.[70] Seemakurthi et al. reported through DFT calculations that the d-band center of Pd in PdIn alloys shifts downward by 0.6 eV relative to pure Pd, weakening propylene adsorption from –0.97 eV to –0.59 eV while simultaneously lowering the activation barrier for propane C–H bond cleavage from 1.26 eV to 0.87 eV. This enables a synergistic optimization of activity and selectivity. Furthermore, they proposed a selectivity descriptor defined as the difference between the effective activation barrier for propane C–H bond activation and that for propyne C–C bond scission, which allows accurate prediction of propylene selectivity in alloy catalysts.

3.4.2 Regulation of Intermediate Adsorption–Desorption Balance

The adsorption strength of propylene and reaction intermediates directly determines selectivity: overly strong adsorption tends to cause deep dehydrogenation or C–C bond cleavage, whereas overly weak adsorption reduces catalytic activity. Density functional theory (DFT) studies achieve a dynamic balance of "adsorption–activation–desorption" by optimizing intermediate adsorption energies.

3.4.2.1 Competition between Propylene Desorption and Deep Dehydrogenation

The essence of propylene selectivity lies in the competition between desorption and deep dehydrogenation. By comparing the energy barriers of these two processes, DFT calculations clarify the direction for selectivity regulation.

DFT studies on Pt–Zn catalysts show that Zn introduction reduces the propylene desorption barrier on Pt(111) from 0.62 eV to 0.31 eV, while increasing the deep dehydrogenation barrier from 0.91 eV to

1.01 eV. Consequently, the barrier difference expands from 0.29 eV to 0.70 eV [Fig. 8], favoring preferential propylene desorption. At the same time, the C–C bond cleavage barrier increases from 0.51 eV to 2.21 eV, further suppressing cracking side reactions.

The selectivity mechanism of RuP catalysts highlights intermediate adsorption optimization. DFT calculations reveal that on the RuP(112) surface, the propylene adsorption energy (−1.567 eV) is stronger than that on Ru(101) (−0.56 eV), yet the propylene desorption barrier (1.81 eV) is much lower than the deep dehydrogenation barrier (3.42 eV), enabling facile desorption. Meanwhile, the adsorption energy of coke precursors such as propyne is weakened from −1.71 eV to −1.59 eV, inhibiting polymerization and deposition. [71]

3.4.2.2 Regulation of Key Intermediate Adsorption

The adsorption strength of key intermediates in propane dehydrogenation, such as propyl and 1-propenyl species, directly affects reaction pathway selection. DFT calculations guide the reaction toward propylene formation by tuning intermediate adsorption energies.

DFT studies on Pt–In single-atom alloys (SAAs) show that isolated Pt sites exhibit a weaker adsorption energy for isopropyl intermediates (−2.95 eV) than Pt nanoparticles (−3.02 eV), while the C–H activation barrier decreases from 0.51 eV to 0.44 eV. This maintains activity while preventing over-adsorption–induced deep dehydrogenation. The weakened adsorption of 1-propenyl intermediates (−2.8 eV vs. −4.46 eV) further suppresses their transformation into coke precursors.

The intermediate regulation mechanism of Cr–Al–O catalysts has also been elucidated.[33] DFT calculations by Li et al. show that Al doping decreases the propyl adsorption energy on Cr_2O_3(0001) from −3.02 eV to −2.95 eV and weakens propylene adsorption from −1.51 eV to −1.33 eV, reducing the risk of deep dehydrogenation. Simultaneously, the C–C bond cleavage barrier increases from 2.1 eV to 3.42 eV, significantly suppressing cracking side reactions.

3.4.3 DFT Studies on Anti-Coking Mechanisms

Coke formation mainly originates from polymerization of alkyne intermediates (e.g., propyne, 1-propynyl) generated via deep dehydrogenation of propylene, or from deposition of C_1/C_2 species produced by C–C bond cleavage. DFT studies reveal coke formation pathways and propose two major anti-coking strategies: “suppressing coke precursor formation” and “promoting coke oxidation/desorption”.

3.4.3.1 Suppression of Coke Precursor Formation

By increasing the energy barriers for deep dehydrogenation and C–C bond cleavage, the formation of coke precursors (e.g., propyne, carbon species) can be reduced at the source.

The anti-coking mechanism of Pt–B modified catalysts focus on inhibiting coke precursor formation. DFT calculations show that Pt–B clusters weaken propyne adsorption from −1.81 eV to −1.70 eV and raise the C–C bond cleavage barrier from 1.73 eV to 2.21 eV. Meanwhile, B introduction increases electron density on Pt sites, lowering the propylene desorption energy from 0.62 eV to 0.38 eV, reducing propylene residence time and subsequent deep dehydrogenation. As a result, the formation rate of coke precursors decreases by more than 60% [Fig. 8(g)-(h)]. [2]

DFT studies on Rh(111) surfaces reveal that coke formation mainly arises from C–C bond cleavage of propyne (barrier 1.98 eV) and polymerization of carbon species (barrier 0.8 eV). With O modification, propyne adsorption weakens from −1.6 eV to −1.1 eV, the C–C cleavage barrier increases to above 2.5 eV, and carbon species preferentially react with O to form CO (barrier 1.2 eV), significantly reducing coke deposition rates.

3.4.3.2 Regulation of Coke Precursor Adsorption and Transformation

Coke deposition can also be mitigated by weakening coke precursor adsorption and promoting their oxidation or desorption [Fig. 8(j)]. The anti-coking mechanism of Pt–In SAA is associated with enhanced

intermediate desorption. DFT calculations show that the adsorption energy of 1-propenyl intermediates on Pt–In SAA (−2.8 eV) is much weaker than on Pt nanoparticles (−4.46 eV), while the deep dehydrogenation barrier to propyne increases from 1.0 eV to 1.5 eV, reducing coke precursor formation.[1] Rapid propylene desorption (0.28 eV) further lowers surface polymerization probability, decreasing coke content from 4.31% on Pt/Al_2O_3 to 0.82% on Pt–In SAA .

The anti-coking mechanism of Cr–Al–O catalysts relies on regulation of surface oxygen species. DFT calculations show that Al doping lowers the oxygen vacancy formation energy on Cr_2O_3 from 1.08 eV to 0.76 eV, enhancing oxygen activity. The reaction barrier for coke precursors (e.g., propyne) with surface oxygen to form CO decreases from 2.3 eV to 1.7 eV, promoting coke oxidation and desorption. Meanwhile, the propylene desorption energy is reduced, further suppressing coke accumulation.

3.4.4 Synergistic Optimization Strategies for Selectivity and Coke Resistance

Density functional theory (DFT) studies demonstrate that propylene selectivity and coke resistance are intrinsically synergistic and can be simultaneously enhanced through multidimensional regulation. The main strategies include:

Bimetallic synergistic regulation.

Through the combined effects of geometric isolation and electronic modulation, such as in Pt–In and Ni–In alloys, continuous metal ensembles are disrupted while the d-band center of the active metal is tuned. This dual regulation simultaneously improves propylene selectivity and suppresses coke formation.

Support acidity and defect engineering.

In Cr_2O_3/Al_2O_3 catalysts, Al doping reduces the density of strong acid sites on the support. DFT calculations show that the adsorption energy of propylene on strong acid sites decreases from −1.8 eV to −1.3 eV, suppressing propylene polymerization and coke formation. Meanwhile, oxygen vacancies promote surface oxygen cycling, accelerating coke oxidation.

Reaction-atmosphere synergy.

DFT studies on H_2 co-feeding reveal that hydrogen competitively adsorbs on Pt–Cu single-atom alloy surfaces (adsorption energy −0.32 eV), occupying part of the active sites. This further weakens propyne adsorption by 0.1–0.2 eV, suppresses C–C bond cleavage, and reduces coke coverage by more than 30%.

3.4.5 Common Mechanistic Principles and Design Implications

Based on DFT studies across different catalyst systems, the mechanisms governing selectivity control and coke resistance exhibit the following common features:

Adsorption-energy balance as the core of selectivity control.

The optimal propylene adsorption energy should lie between −0.4 eV and −0.6 eV, which ensures sufficient C–H bond activation while avoiding excessive adsorption that leads to deep dehydrogenation and side reactions.

Dual suppression strategy for coke resistance.

Coke resistance relies on two complementary mechanisms:

(1) suppressing the formation of coke precursors by increasing the energy barriers for deep dehydrogenation and C–C bond cleavage;

(2) promoting the desorption or conversion of coke precursors by weakening their adsorption or introducing oxidative active sites.

Single-site principle for active-site design.

Isolated and uniform active sites—such as single atoms or well-defined dual-atom sites—are more favorable for achieving both high selectivity and stability, as they suppress multi-atom-assisted cracking and polymerization reactions.

These insights provide clear guidance for catalyst design. For Pt-based catalysts, forming single-atom alloys with elements such as Cu or In can tune the d-band center and enhance site isolation. For non-noble Ni-based catalysts, alloying with In or Zn can increase Ni–Ni separation and optimize Ni–C interactions.

For Cr-based catalysts, Al doping can regulate oxygen vacancies and surface acidity to improve both selectivity and coke resistance. All these strategies have been validated by DFT calculations in terms of thermodynamic and kinetic feasibility, offering a solid theoretical foundation for the development of highly efficient PDH catalysts.

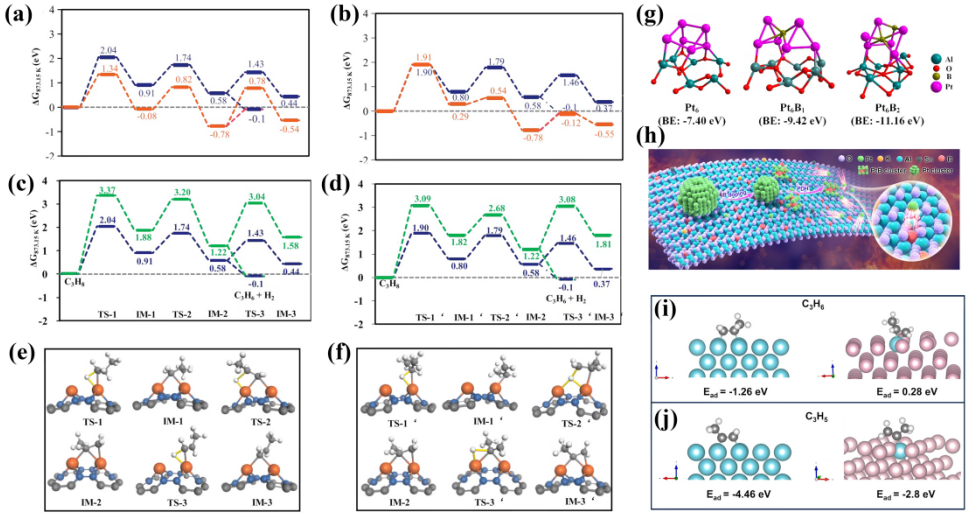

Figure 8. Potential energy surfaces of PDH reaction at 873.15 K via C_3H_8 → 1-C_3H_7*(IM-1) → C_3H_6* → 1-C_3H_5*(IM-3)) on Sc_2@NG (a, orange color) and Ni_2@NG (c, green color), respectively; Potential energy surfaces of PDH reaction at 873.15 K via C_3H_8 → 2-C_3H_7*(IM-1′) → C_3H_6* → 2- C_3H_5*(IM-3′) on Sc_2@NG (b, orange color) and Ni2@NG (d, green color), respectively; The Pt (111) surface was used as a comparison (blue color). Intermediate and transition state structures on Sc2@NG (blue ball for N, grey ball for C, white ball for H and orange ball for Sc).Structures and adsorption energies of the adsorbates C_3H_6 (i) and C_3H_5 (j) on Pt NPs and Pt–In SAA models.(g) Optimized lowest-energy cluster structures of pure Pt6, Pt6B1, and Pt_6B_2 and their corresponding binding energy on θ-$Al2O_3$ (010). Note: For simplicity, K and Sn atoms were hided. (h) Possible redispersion mechanism of Pt species on PtSnK-B0.32.

3.5 Surface Structure and Identification of Active Sites

The activity, selectivity, and stability of propane dehydrogenation (PDH) reactions strongly depend on the catalyst surface structure and on the geometric configuration, electronic state, and coordination environment of active sites. Density functional theory (DFT) enables the construction of accurate surface models, calculation of intermediate adsorption energies and reaction barriers, and, when combined with microkinetic analysis, reveals the intrinsic structure–activity relationships of active sites in different catalyst systems. Based on DFT studies of Pt-based, Ga-based, Zr-based, and other catalysts, this section systematically summarizes surface structure regulation mechanisms and active-site identification strategies.

3.5.1 Surface Structures and Active Sites of Metal and Alloy Catalysts

The surface structure of metal and alloy catalysts (crystal facets, defects, interatomic distances) directly determines the nature and performance of active sites. DFT studies identify key active sites by comparing catalytic behaviors on different facets and alloy compositions.

3.5.1.1 Facet-Dependent Characteristics of Active Sites

Differences in atomic arrangement and coordination number among crystal facets significantly influence PDH reaction pathways and energy barriers. DFT calculations clearly identify favorable facets and corresponding active sites.

For Pt-based catalysts, DFT combined with Bayesian analysis confirms that Pt(211) step surfaces and Pt(111) terrace surfaces are the primary active facets, whereas Pt(100), which readily induces cracking side reactions, is excluded as a dominant active surface [Fig. 9(a)]. [18] Step sites on Pt(211) lower the energy barrier for the first dehydrogenation step of propane to 1.45 eV, and the barrier for the selectivity-determining step (1.80 eV) is significantly lower than that for cracking reactions. In contrast, Pt(111) terrace sites exhibit a slightly higher dehydrogenation barrier (1.74 eV) but superior stability.

Comparative DFT calculations on Pt(111), Pt(100), Pt(110), and Pt(211) surfaces show that Pt(110), owing to its moderate atomic packing density, achieves an optimal balance between adsorption of isopropyl intermediates (−1.30 eV) and dehydrogenation barriers (1.29 eV), making it the most kinetically active facet.[8] Although Pt(211) step sites further reduce the second dehydrogenation barrier (to 0.22 eV), they are easily covered by hydrogen species (coverage up to 42%), which suppresses the effective activity .

For RhCu single-atom alloys, dilution of Rh atoms by Cu on the Rh(111) surface forms isolated Rh sites. DFT calculations show that the propane C–H activation barrier decreases from 1.98 eV to 1.42 eV while deep dehydrogenation of propylene is suppressed, demonstrating the advantage of isolated terrace-site active centers.

3.5.1.2 Active-Site Reconstruction via Alloying

Bimetallic alloying reconstructs active sites through combining geometric isolation and electronic modulation. DFT studies clarify structure–activity relationships between alloy composition and active sites.

In Pt–Zn alloys, the active sites are identified as isolated Pt atoms. Zn incorporation increases the Pt–Pt distance from 2.77 Å to 3.12 Å, breaking contiguous Pt ensembles, and shifts the Pt d-band center downward from −2.21 eV to −2.43 eV. Consequently, propylene adsorption weakens from −0.89 eV to −0.47 eV, effectively suppressing deep dehydrogenation [Fig. 9(c)-(e)].[27]

For Ga–Pt alloys, DFT calculations identify isolated Pt atoms embedded in a liquid Ga matrix as the active sites. These Pt atoms carry a negative charge (−0.68 e), and electronic interactions with Ga lower the propane dehydrogenation barrier to 0.61 eV. CO adsorption experiments confirm that Pt remains atomically isolated under reaction conditions without aggregation.[43]

In Ni–In alloys, DFT demonstrates that increasing In content expands the Ni–Ni distance from 2.479 Å to 3.177 Å, generating isolated Ni sites. This increases the propylene deep-dehydrogenation barrier from 0.8 eV to 1.2 eV, establishing the “degree of isolation” as a key descriptor for active-site design.[58]

3.5.2 Surface Structures and Active Sites of Oxide and Composite Oxide Catalysts

In oxide catalysts, active sites are commonly associated with the coordination environment of metal cations and oxygen vacancies. DFT studies reveal how cation valence states, coordination numbers, and support modifications regulate active sites.

3.5.2.1 Active Sites Regulated by Cation Coordination Environment

The coordination number of metal cations on oxide surfaces directly affects catalytic activity, with DFT calculations identifying low-coordination cations as the core active sites.

For Ga_2O_3 catalysts, the active sites are identified as tetrahedrally coordinated, low-coordination Ga^{3+} species ([$HGaO_3$] configuration). DFT optimization shows Ga–O bond lengths of 1.98 Å, shorter than those in six-coordinated Ga^{3+} sites. These sites more readily activate H_2 to form Ga–H intermediates [Fig. 9(b)], lowering the propane dehydrogenation barrier to 0.70 eV. Ga–H species act as key intermediates in C–H bond activation.

For Zr-based composite oxides, DFT identifies $Zn_{(cus)}$–O–$Zr_{(cus)}$ dual sites as the active centers. Zn doping induces oxygen vacancies on ZrO_2 surfaces, converting Zr^{4+} into coordinatively unsaturated $Zr_{(cus)}$ species. Synergistic interaction between $Zn_{(cus)}$ and $Zr_{(cus)}$ sites lowers the first and second dehydrogenation barriers of propane to 0.61 eV and 0.52 eV, respectively—significantly lower than those on single $Zr_{(cus)}$ or $Zn_{(cus)}$ sites.[48]

For Cr_2O_3-based catalysts, DFT identifies Pt single-atom-modified Cr–O ion pairs as the true active sites. Substitution of Cr by Pt single atoms lowers the conduction band minimum (CBM) of neighboring oxygen atoms from −0.8 eV to −1.2 eV, enhancing hydrogen capture capability and reducing the first propane dehydrogenation barrier from 1.57 eV to 1.13 eV.[32]

3.5.2.2 Active-Site Regulation via Oxygen Vacancies and Support Modification

Oxygen vacancies and support doping optimize catalytic performance by modifying the electronic states of active sites.

For $ZnZrO_x$ composite oxides, DFT calculations show that Zn doping reduces the oxygen-vacancy formation energy on ZrO_2 surfaces from 1.36 eV to 0.98 eV.[48] Increased electron density around $Zr_{(cus)}$ sites near vacancies weakens the C–H activation barrier and enhances oxygen mobility, thereby suppressing coke formation.

In Al-doped Cr_2O_3 catalysts, DFT reveals that Al incorporation reduces the coordination number of Cr^{3+} from six to five, generating low-coordination Cr active sites. Propane adsorption strengthens from −0.38 eV to −0.52 eV, while the C–H activation barrier decreases from 2.1 eV to 1.8 eV, with simultaneous suppression of C–C bond cleavage.

For Pt single-atom-modified Cr_2O_3, strong interactions between Pt atoms and surrounding oxygen (Pt-5d/O-2p orbital coupling) reconstruct the electronic structure of Cr–O sites, enhancing hydrogen capture. As a result, the propane dehydrogenation rate increases by a factor of three, and Pt single atoms remain atomically dispersed under both reaction and regeneration conditions (formation energy −1.2 eV).[32]

3.5.3 Identification of Active Sites in Single-Atom and Single-Atom Alloy Catalysts

Single-atom and single-atom alloy catalysts possess well-defined isolated atomic active sites. DFT precisely reveals the relationships among geometric structure, electronic state, and catalytic performance.

3.5.3.1 Characteristics of Active Sites in Single-Atom Catalysts

In single-atom catalysts, the active site consists of an isolated metal atom, and its coordination environment is the key factor governing performance. DFT calculations clarify the relationship between ligand type and activity.

For Ir single-atom catalysts, the active site is identified as an Ir–O_2N_2 coordination configuration. DFT calculations show that the Ir atom carries a charge of +0.42 e, and mixed N/O coordination lowers the first propane dehydrogenation barrier (2.00 eV) relative to Ir–N_4 sites (2.24 eV). Moreover, the second dehydrogenation step changes from endothermic (+0.35 eV) to exothermic (−0.33 eV), providing a clear thermodynamic advantage.[13]

For Pt single-atom catalysts, the active sites are isolated Pt atoms substituting Cr sites. DFT calculations show that Pt coordinates with four surrounding oxygen atoms, and strong coupling between Pt-5d and O-2p orbitals enhances the activity of neighboring Cr–O sites. As a result, the propane dehydrogenation turnover frequency (TOF) is increased by an order of magnitude compared with pure Cr_2O_3.[32]

3.5.3.2 Characteristics of Active Sites in Single-Atom Alloys

The active sites of single-atom alloys consist of isolated noble-metal atoms dispersed within a host metal matrix, and DFT studies have clarified the synergistic contributions of geometric isolation and electronic

modulation. For Pt–Cu single-atom alloys, combined DFT and kMC simulations confirm that isolated Pt atoms serve as the active centers. The geometric isolation imposed by the Cu matrix increases the Pt–Pt distance to above 3.0 Å, suppressing propylene polymerization, while electron transfer shifts the Pt d-band center downward, weakening propylene adsorption from –0.65 eV to –0.47 eV and doubling the desorption rate.[9]

For RhCu single-atom alloys, DFT identifies isolated Rh atoms as the active sites. The introduction of Cu reduces the coordination number of Rh from 9 to 1, lowering the activation barrier for propane C–H bond cleavage from 1.87 eV to 1.42 eV. Meanwhile, the adsorption energy of the coke precursor (propyne) decreases from –1.6 eV to –1.1 eV, leading to significantly enhanced resistance to coking.

3.5.4 DFT Methodologies and Key Descriptors for Active-Site Identification

DFT, combined with microkinetic analysis and electronic-structure calculations, has established core methodologies and key descriptors for identifying active sites, providing quantitative guidance for catalyst design.

3.5.4.1 Core Methodologies for Active-Site Identification

Energy-barrier and adsorption-energy analysis: By calculating intermediate adsorption energies and reaction barriers at different sites, the most favorable active centers can be identified. For example, Pt(211) step sites are recognized as active centers due to their lowest dehydrogenation barriers.

Electronic-structure analysis: Calculations of the d-band center, charge-density difference, and projected density of states (PDOS) reveal the electronic interactions between active sites and intermediates. For instance, the downward shift of the Pt d-band center in Pt–Zn alloys is the key factor responsible for weakened propylene adsorption.

Microkinetic validation: Kinetic models constructed from DFT-derived energetics verify the actual contribution of proposed active sites. For example, microkinetic simulations of Pt-modified Cr_2O_3 show that the TOF of Cr–O sites agrees well with DFT-predicted barriers, confirming their role as active centers.

3.5.4.2 Key Structural and Electronic Descriptors

Geometric descriptors:

Interatomic distance: A critical indicator of isolated sites in alloys (e.g., Ni–Ni distances ≥ 3.0 Å in Ni–In alloys).

Coordination number: Low-coordination cations exhibit higher activity (e.g., Ga with CN = 4 in Ga_2O_3).

Oxygen-vacancy concentration: In Zr-based oxides, an oxygen-vacancy formation energy ≤ 1.0 eV is the threshold for effective active-site formation.

Electronic descriptors:

d-band center: For metal catalysts, a d-band center between –2.0 and –2.5 eV balances activity and selectivity.

Charge density: Cations with charges of +3 to +4 in oxides more readily activate C–H bonds.

Conduction-band minimum (CBM): When the O-atom CBM ≤ –1.0 eV, hydrogen-capture capability is enhanced.

3.5.5 Structure–Activity Relationships and Design Implications

DFT studies across diverse catalyst systems reveal several universal correlations between surface structure and active-site behavior:

Isolated active sites are the foundation of high selectivity.

Whether isolated metal atoms in alloys, low-coordination cations in oxides, or single-atom catalytic centers, isolated sites suppress cracking and polymerization pathways that require multi-atom ensembles.

Electronic-state modulation is essential for optimizing activity.

Alloying or support modification can tune the d-band center or charge density of active sites, enabling precise control of intermediate adsorption strengths and balancing activity with selectivity.

Synergistic site design enhances catalytic performance.

Dual sites in mixed oxides (e.g., Zncus–O– Zncus) or host–guest cooperation in single-atom alloys can lower multiple reaction barriers simultaneously, enabling performance breakthroughs [Fig. 9(d)].

DFT provides clear guidance for active-site engineering:

For metal catalysts: prioritize step surfaces or construct isolated sites via alloying.

For oxide catalysts: focus on low-coordination cations and oxygen-vacancy synergy.

For single-atom catalysts: optimize N/O coordination to balance electronic structure and stability.

These strategies, validated by DFT through both thermodynamic and kinetic analyses, offer a robust theoretical foundation for the rational design of high-performance PDH catalysts.

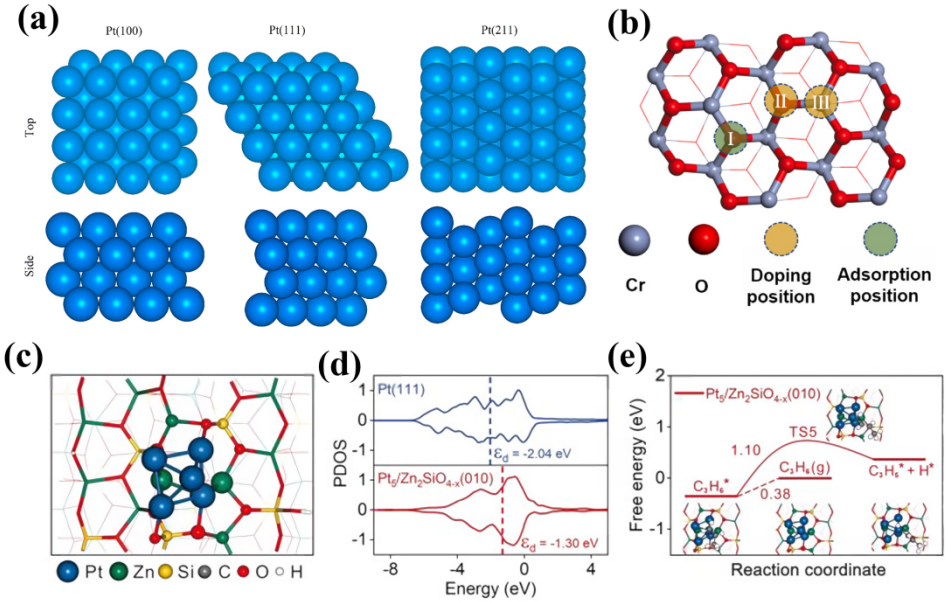

Figure 9. (a)Schematics of all platinum facets used in this study (b). Pt atom position of Cr_2O_3(0001). (b) optimized model of a tetra-coordinated Ga−H on the surface of Ga_2O_3 by H2 dissociation. DFT calculation on the PDH process at Pt−ZnOx interfaces. (c) Top view of the Pt_5/Zn_2SiO_4-x(010) model. (d) Reaction mechanisms of PDH on Pt_5/Zn_2SiO_4-x(010) (red) and Pt(111) (blue). Bottom: the configurations of the reaction intermediates on the Pt_5/Zn_2SiO_4-x(010) model. (e) The partial density of states of Pt 5d orbitals on Pt(111) and Pt_5/Zn_2SiO_4-x(010), respectively. The Fermi level was set to zero.

4. Applications of Multiscale Modeling and Machine Learning in Propane Dehydrogenation

4.1 Microkinetic Modeling

Microkinetic modeling—including kinetic Monte Carlo (kMC) simulations and mean-field microkinetic models—uses adsorption energies and reaction barriers obtained from density functional theory (DFT) to construct complete reaction networks. These models quantitatively describe reaction rates, surface coverages of intermediates, and product selectivity as functions of reaction conditions, serving as a critical bridge between atomistic catalyst structures and macroscopic catalytic performance. This section

systematically summarizes the applications and key insights of microkinetic simulations in propane dehydrogenation (PDH), with representative examples from Pt-, Pd-, Cr-, and Co-based catalyst systems.

4.1.1 Construction of Reaction Networks and Identification of Key Steps

The core of microkinetic modeling lies in building a comprehensive reaction network that includes main reactions, side reactions, and adsorption–desorption steps, and then identifying performance-limiting elementary steps through degree of rate control (DRC) analysis.

4.1.1.1 Pt-based catalysts

By combining DFT with kMC simulations, researchers constructed a PDH reaction network containing 54 reversible elementary steps, covering adsorption, desorption, C–H bond scission, and C–C bond cleavage. The results show that the first C–H activation step forming 1-propyl is the rate-determining step (barrier ≈ 1.16 eV), while the high barriers for propylene deep dehydrogenation (1.29–1.30 eV) are responsible for the high selectivity toward propylene.[9] Mean-field microkinetic models further confirmed that on Pt(211) step sites, the first dehydrogenation (1.45 eV) and the selectivity-determining step (1.80 eV) dominate the reaction, with hydrogen species identified as the most abundant surface intermediates (MASI).[18]

4.1.1.2 Pd-based catalysts

For PdIn alloys, a microkinetic model incorporating 39 surface species and 52 surface reactions was developed. DRC analysis revealed that C–H bond cleavage of propane to form 1-propyl is the key rate-controlling step for propylene formation (DRC = 0.72), whereas C–C bond cleavage of propyne (DRC = 0.96) governs methane formation, providing a kinetic basis for selectivity descriptors.[70]

4.1.1.3 Cr-based catalysts

Based on 74 DFT-derived elementary steps, kMC simulations distinguished the mechanisms on reduced and oxidized α-Cr_2O_3(0001) surfaces. On reduced surfaces, C–H activation (1.25–1.27 eV) is rate-limiting, while oxidized surfaces follow a Mars–van Krevelen mechanism [Fig. 10(a)], where H_2O formation and desorption (1.19–1.36 eV) significantly affect kinetics. [31]

4.1.1.4 Co-based catalysts

Microkinetic modeling showed that PDH on FCC-Co(111) proceeds via both 1-propyl and 2-propyl pathways, whereas HCP-Co(0001) preferentially follows the 1-propyl route. In both cases, the first C–H bond scission is rate-determining, with barriers of 0.66 eV (FCC) and 1.05 eV (HCP), respectively.[59]

4.1.2 Quantitative Analysis of Performance Regulation Mechanisms

Microkinetic simulations quantify surface coverages and rate competitions, enabling mechanistic understanding of how geometric effects, electronic effects, and reaction conditions regulate activity, selectivity, and stability.

4.1.2.1 Correlation Between Active-Site Structure and Performance

Single-atom alloys and alloying effects

kMC simulations show that in Pt/Cu single-atom alloys, isolated Pt sites exhibit C–C cleavage barriers consistently above 2.0 eV, much higher than C–H activation barriers (< 1.54 eV), effectively suppressing cracking reactions. Meanwhile, the forward rates of propylene deep dehydrogenation are lower than the reverse rates, maintaining high propylene selectivity.[9] Mean-field microkinetic analysis combined with DFT further demonstrated that in Pt_3Ga and Ni_3Ga alloys, Ga induces geometric isolation and d-band center downshifts, optimizing the adsorption energies of C_3H_6 and H (used as activity descriptors) and making Ni_3Ga superior to pure Ni in both activity and selectivity.[12]

Crystal-phase sensitivity

Microkinetic modeling quantitatively compared FCC-Co and HCP-Co phases. FCC-Co(111) exhibits a higher propylene formation rate (TOF ≈ 0.5 $site^{-1}$ s^{-1}), whereas HCP-Co(0001), due to a lower propylene desorption barrier (1.37 eV vs 2.25 eV), shows superior selectivity (~ 96%) and better coke resistance, providing guidance for phase engineering of Co catalysts.[59]

4.1.2.2 Simulation of Reaction-Condition Effects

Hydrogen co-feeding

kMC simulations indicate that H_2 co-feeding (C_3H_8/H_2 = 1:1) enhances the forward dehydrogenation rate of propane while suppressing forward deep dehydrogenation of propylene, reducing surface carbonaceous species and increasing propane conversion.[9] Mean-field models further show that H_2 co-feeding lowers hydrogen coverage on Pt(111), weakens propylene adsorption, increases propylene selectivity by ~ 4 %, and raises TOF by two orders of magnitude .

Temperature and pressure effects

kMC simulations over 700–900 K and 0.001–40 bar reveal that on oxidized Cr_2O_3 surfaces, propylene selectivity decreases sharply with increasing oxidant pressure (e.g., O_2 > 0.3 bar reduces selectivity to ~ 20%), whereas increasing propane pressure (> 10 bar) enables mixed surfaces (oxidized + reduced) to achieve propylene selectivity above 90 % [Fig. 10]. [31] Pressure-dependent analyses further indicate that optimal activity on Pt-based catalysts corresponds to C_3H_6 formation energies of 0.2–0.5 eV, while overly strong H adsorption suppresses activity. [12]

4.1.3 Suppression of Side Reactions and Catalyst Stability

Microkinetic modeling enables quantitative evaluation of deep dehydrogenation, cracking, and coke formation, thereby elucidating catalyst deactivation mechanisms.

Coke formation pathways.

kMC simulations reveal that on Pt catalysts, propyne is the primary coke precursor. Its C–C cleavage (≈ 1.37 eV) generates C_1/C_2 species that polymerize into coke. In contrast, on Pt/Cu single-atom alloys, coke mainly originates from deep dehydrogenation of intermediates such as CH_3CCH_2 and CH_3CHCH rather than C–C scission, and H_2 co-feeding suppresses coke by lowering the coverage of these intermediates.[9]

Oxidation-state regulation.

Microkinetic studies confirm the existence of an optimal surface oxidation degree for Cr_2O_3 catalysts (≈ 0.2 with O_2 and ≈ 0.5 with N_2O as oxidants), at which propylene yield is maximized. Using N_2O as a soft oxidant lowers the apparent deactivation activation energy (0.81 eV vs 1.70 eV for O_2), because N_2O-derived oxygen species more effectively suppress coke formation.[31] Simulations of Pt_4 clusters confined in Fe-MFI zeolites further show that high C–C cleavage barriers (2.37–2.72 eV) and higher barriers for propylene deep dehydrogenation than for desorption kinetically suppress side reactions and deactivation.[68]

4.1.4 Methodological Advances in Microkinetic Modeling

Multiscale coupling approaches integrate DFT+U calculations—which account for strong electronic correlation effects—with kMC simulations to capture catalyst structural dynamics under realistic reaction conditions. By incorporating surface redox transitions (oxidized ↔ reduced states) and oxygen-vacancy migration (barrier: 0.63 eV), these methods enable accurate simulation of the dynamic evolution of catalyst surfaces.[31]

By combining DFT with kMC simulations, the influence of hydrogen coverage on reaction kinetics has been quantitatively evaluated; for example, the H coverage on Pt(211) surfaces can reach 42%, and incorporating this effect corrects the barrier deviations that arise when coverage is neglected.

Descriptor-driven model simplification: Microkinetic simulations have been used to simplify complex reaction networks, leading to the proposal of a selectivity descriptor defined as the effective free-energy difference between propane C–H bond cleavage and propyne C–C bond scission. This descriptor accurately predicts propylene-selectivity trends for various alloys such as PdZn and PdIn, achieving higher correlation coefficients (R^2) than traditional descriptors.[70]

Based on microkinetic datasets, it has been further demonstrated that the formation energies of C_3H_6 and H can serve as activity descriptors, while the C_3H_6 formation energy alone functions as a selectivity descriptor ($R^2 = 0.94$), providing a simplified framework for high-throughput catalyst screening.[12]

4.1.5 Applications and Limitations

The main strengths of microkinetic modeling include:

(1) Quantitative validation of DFT-derived structure–performance relationships and active-site identification (e.g., isolated Pt sites in Pt/Cu SAAs and Cr^{3+} sites in Cr_2O_3);

(2) Optimization of reaction conditions (temperature, pressure, H_2 co-feeding) for industrial guidance;

(3) Identification of side-reaction-controlling steps to guide the design of coke-resistant, highly selective catalysts .

However, limitations remain:

(1) Strong dependence on the accuracy of DFT energetics, with functional errors propagating into kinetics;

(2) Necessary simplifications of reaction networks, which may neglect minor pathways relevant to long-term stability;

(3) Lattice-based kMC models cannot fully capture the complexity of real catalyst surfaces with defects and dynamic restructuring.

Future developments should integrate multiscale modeling with operando characterization data, apply machine learning to correct DFT energy errors, and extend reaction networks to include catalyst sintering and coke evolution for long-term deactivation prediction.

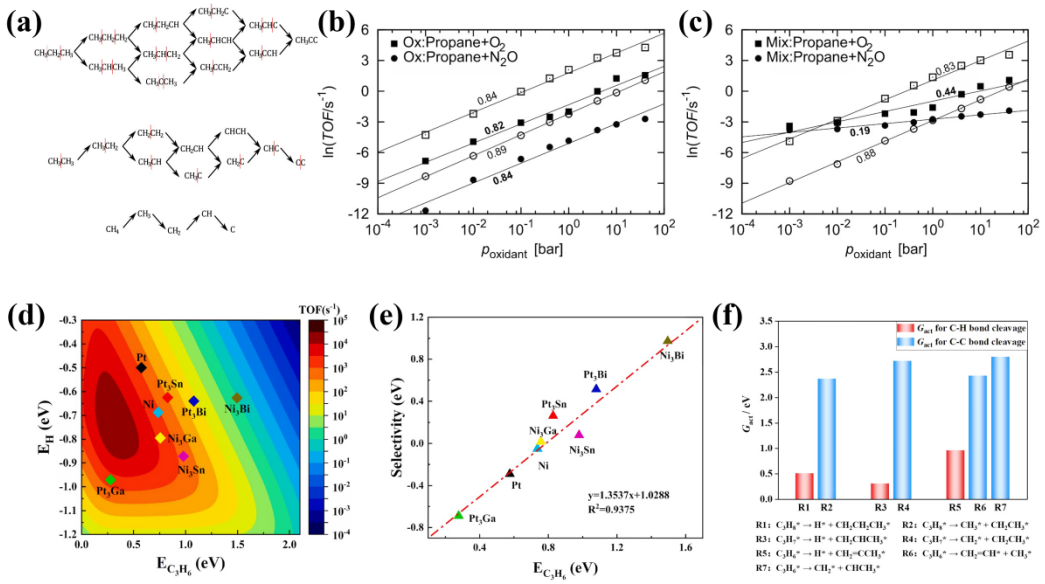

Figure 10. (a)Schematic representation of the reaction mechanism with all carbon intermediates. Black arrows represent (de)hydrogenation reaction steps (all reactions are considered reversible in the model) and red lines represent a possible C−C cleavage. Dotted lines represent cleavages that are accounted for due to symmetry. TOF for the dehydrogenation of propane at $pCH_3CH_2CH_3$ = 1.0 bar and T = 900 K and various oxidant types and pressures on the oxidized(b) and mixed(c) surface. The mixed surface consists of 50% of the oxidized and 50% of the reduced surfaces and includes diffusion of the intermediates across the phase boundary. The symbol shape denotes the oxidant used: ■ O_2 and ● N_2O. Full symbols denote propene production and empty symbols denote CO_2 production. Inset values denote the slopes, which correspond to the reaction order with respect to the oxidant.(d) The activity volcano map of PDH as a function of EH and

EC_3H_6 (formation energies of adsorbed H and C_3H_6), (e) linear scaling correlation between propylene selectivity (indicated by ΔE = Edeep − Edes) (f)Comparison of the activation barriers calculated for C−C/C−H bond cleavage of C_3H_8, C_3H_7 and C_3H_6 species over Pt_4/FeMFI.

4.2 Reactive Force Fields and Molecular Dynamics Simulations

Reactive force fields (e.g., ReaxFF, Deep Potential) combined with molecular dynamics (MD) simulations overcome the limitations of DFT in system size and simulation timescale. They enable atomistic descriptions of bond breaking/formation, intermediate evolution, and catalyst surface dynamics during propane dehydrogenation (PDH), providing efficient multiscale tools for mechanism elucidation and catalyst optimization.

4.2.1 Development and Validation of Reactive Force Fields

The reliability of MD simulations depends on the accuracy of reactive force fields, which are trained on DFT datasets covering intermediate structures, adsorption energies, and activation barriers.

Pt-based catalyst ReaxFF development: A 2023-Pt/C/H ReaxFF force field was developed for Pt-catalyzed PDH.[14] The training set included key DFT data for PDH reaction networks on Pt(111), such as adsorption energies of propane and propylene, relative energies of 1-propyl and 2-propyl intermediates, and energy profiles for C–H activation and C–C cleavage, totaling 14,365 structures. Internal validation showed mean absolute errors (MAEs) of 14 $kJ \cdot mol^{-1}$ for intermediate energies and 12 $kJ \cdot mol^{-1}$ for reaction barriers, closely matching DFT results. External validation confirmed accurate reproduction of barrier trends on Pt(100) and Pt(211), enabling large-scale simulations of structure sensitivity in Pt catalysts .

Deep learning force field development: A Deep Potential force field for oxidative dehydrogenation (ODH) was constructed using a concurrent learning strategy.[15] ReaxFF MD pre-sampling generated 3.25 million C/H/O-containing cluster structures, which were labeled by DFT calculations. The trained model achieved energy MAEs of 0.03 eV/atom (training) and 0.10 eV/atom (test), and a force MAE of 0.13 eV/Å, accurately capturing the dynamic evolution of short-lived radicals in gas-phase ODH .

4.2.2 Catalyst Surface Structure Sensitivity and Reaction Kinetics

Reactive force-field MD simulations enable efficient exploration of how catalyst surface topologies—such as facets, steps, and defects—affect PDH activity and selectivity, allowing quantitative comparison of reaction behavior across different surface sites.

MD simulations of facet effects on Pt surfaces: Using the 2023-Pt/C/H reactive force field, MD simulations reveal that the PDH activity of Pt catalysts is strongly dependent on surface topology, with the reactivity order Pt(111) < Pt(100) < Pt(211). The low-coordination Pt atoms at the Pt(211) step surface serve as the primary active sites, where propane preferentially undergoes C–H bond activation (Fig. 7). The reaction rate at the step site is 1.4 times that on the flat Pt(111) terrace. In terms of selectivity, Pt(211) exhibits the highest propylene yield (≈25%), whereas Pt(111) shows only 13% propylene selectivity due to its greater propensity for C–C bond-scission side reactions [Fig. 11].

The simulations further show that at elevated temperatures (773–1073 K), Pt surfaces rapidly deactivate due to adsorption of C_1/C_2 species formed via deep dehydrogenation, and the deactivation rate increases significantly with temperature—consistent with experimentally observed high-temperature deactivation of Pt catalysts.[14]

Dynamic-structure simulations of single-atom alloys (SAAs): Machine-learning interatomic potentials combined with MD simulations have been employed to investigate the dynamic structural evolution of Rh–Cu and Pd–Cu SAA nanoparticles.[72] The simulations show that Rh dopant atoms occupy almost exclusively (111) surface sites at 400–600 K, whereas Pd dopants distribute across (111), (100), (110), and interfacial sites. Increasing temperature promotes Rh migration from the bulk to the surface, while Pd tends to diffuse into the bulk but simultaneously increases its occupancy of low-coordination surface sites.

This dynamic redistribution of dopant atoms directly influences catalytic activity. Low-coordination SAA sites—such as (211) steps and (100)–(110) interfacial regions—exhibit significantly lower C–H activation barriers than (111) terrace sites. In Rh–Cu SAAs, the reactivity of Rh atoms adsorbed at (111) surface sites is 100 times higher than that of Rh atoms located on (111) terraces, providing theoretical guidance for site engineering in SAA catalysts.

4.2.3 Reaction Mechanisms and Dynamic Evolution of Intermediates

MD simulations capture real-time formation, transformation, and annihilation of intermediates, revealing dynamic pathways inaccessible to static calculations.

Gas-phase ODH simulations based on Deep Potential MD identified 131 species and 934 elementary reactions.[15] Propane activation initiates via C–C bond cleavage rather than direct C–H breaking, generating methyl and ethyl radicals. Propylene selectivity depends on n-propyl radical pathways: 44 % undergo intramolecular H-shift to isopropyl followed by dehydrogenation to propylene, 44 % undergo C–C cleavage to ethylene, and only 12% directly dehydrogenate. Simulations also reveal an O_2-driven radical chain cycle ($O_2 \rightarrow \cdot OOH \rightarrow H_2O_2 \rightarrow \cdot OH \rightarrow$ propane dehydrogenation) that accelerates reaction rates.

MD tracking of Pt-surface PDH shows the pathway: propane adsorption → C–H activation to propyl → secondary C–H activation to adsorbed propylene → desorption or deep dehydrogenation. [14] Side reactions arise from deep dehydrogenation to propenyl/propyne and C–C cleavage to C_1/C_2 species, which act as coke precursors. Arrhenius analysis yields an apparent activation energy of 73 $kJ \cdot mol^{-1}$, consistent with experimental values for Pt/Al_2O_3 catalysts.

4.2.4 Catalyst Deactivation Mechanisms and Stability Analysis

MD simulations dynamically capture coke formation and surface reconstruction during catalyst deactivation.

Mechanism of coke formation on Pt surfaces: Simulations show that coke formation on Pt surfaces originates from deep dehydrogenation and C–C bond-scission side reactions during PDH. Deep-dehydrogenation intermediates such as propyne and 1-propyl species further decompose into CH_3* and C_2H_5* fragments, which polymerize on the surface to form graphitic-like carbon species that progressively block active sites. C_1/C_2 fragments generated from C–C bond scission diffuse and aggregate on the surface, accelerating coke growth.[14]

The coking rates on different Pt surfaces follow the same trend as their intrinsic activity. Pt(211), which exhibits the highest reactivity, also shows the highest coke coverage (49.4 %) [Fig. 11], whereas Pt(111) exhibits only 26.2 % coverage. This reveals the inherent trade-off between activity and stability.

Dynamic stability of single-atom alloys (SAAs): MD simulations show that the stability of SAA catalysts is closely linked to the dynamic distribution of dopant atoms. [72] In Rh–Cu SAAs, Rh atoms preferentially occupy bulk and (111) surface sites, with a surface occupancy of only 1% at 400 K, resulting in low sensitivity to coking. In contrast, Pd atoms in Pd–Cu SAAs exhibit a high surface occupancy of up to 86 % at 400 K, and their low-coordination surface sites readily adsorb intermediates, making them more prone to coking. However, at elevated temperatures, Pd atoms diffuse into the bulk, partially mitigating deactivation.

Simulations further confirm that tuning the size and morphology of SAA nanoparticles can alter the site distribution of dopant atoms, thereby enabling optimization of long-term catalyst stability.

4.2.5 Methodological Advantages and Application Expansion

Breakthroughs in system size and simulation timescales: Reactive force-field MD simulations can handle systems containing thousands to tens of thousands of atoms, with accessible simulation timescales ranging from nanoseconds to microseconds. For example, a simulation system containing 1840 atoms (160 propane molecules + 40 O_2 molecules) successfully captured the complete reaction cycle of gas-phase ODH

within 150 ps. Similarly, a Pt surface model with 288 surface atoms was simulated for 2 ns, revealing the dynamic process of catalyst deactivation—capabilities that are difficult to achieve using DFT.[14]

Adaptability across diverse reaction scenarios: The flexibility of reactive force fields enables their application to various PDH systems, including metal-catalyzed PDH, single-atom alloy catalysis, and gas-phase oxidative dehydrogenation. For instance, the ReaxFF force field excels at describing bond-breaking and bond-forming events on metal surfaces, whereas Deep Potential force fields, powered by machine-learning models, accurately capture the evolution of short-lived radical intermediates in gas-phase reactions. Together, these tools provide a unified framework for mechanistic studies across multiple PDH environments.

Integration with experimental observations: Simulation results can be directly benchmarked against experimental data. For example, the Pt surface reactivity order and apparent activation energies predicted by the 2023-Pt/C/H force field are consistent with experimental measurements. Deep Potential simulations also reveal the dependence of propylene selectivity on contact time in gas-phase ODH, offering theoretical guidance for optimizing space velocity in experiments.

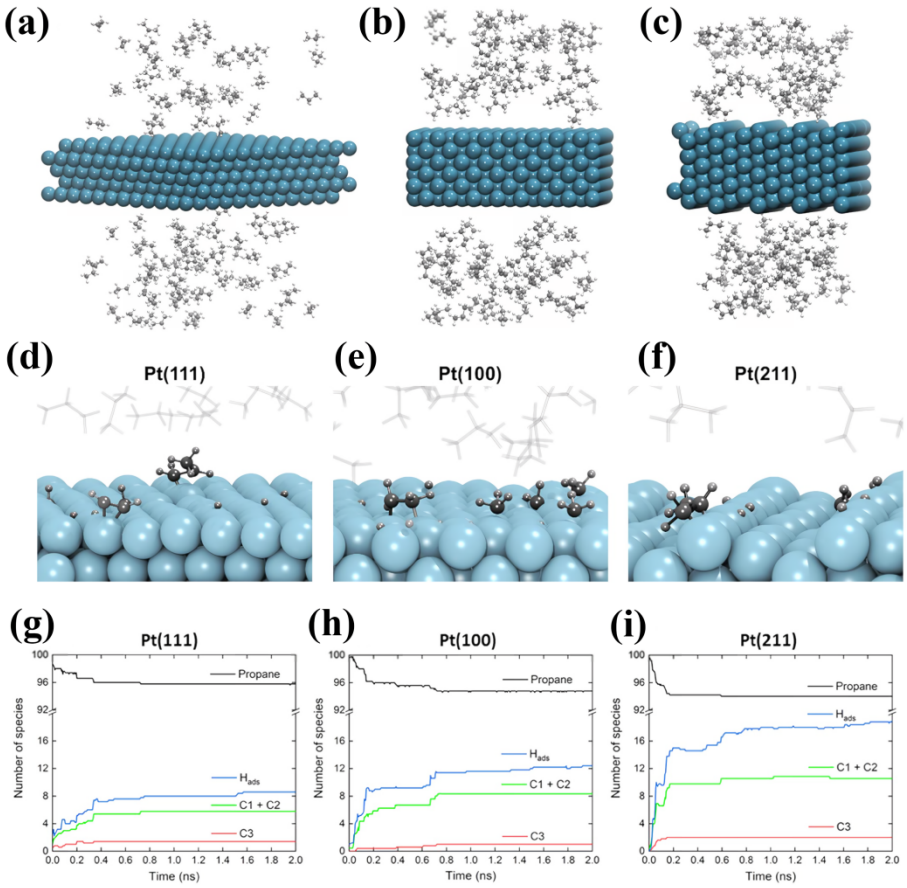

Figure 11. Initial configurations of selected systems to simulate PDH with ReaxFF reactive MD using the 2023-Pt/C/H force field: (a) Pt(111) surface, (b) Pt(100) surface, (c) Pt(211) surface. Illustrative snapshots of the formation of deep dehydrogenated and cracked species on Pt(111) (d), Pt(100) (e), and Pt(211) (f) surfaces during ReaxFF simulations. Initial configurations of selected systems to simulate PDH with ReaxFF reactive MD using the 2023-Pt/C/H force field: (g) Pt(111) surface, (h) Pt(100) surface, (i) Pt(211) surface.

4.3 Machine Learning-Assisted Catalyst Design

Machine learning (ML), with its capability to efficiently process high-dimensional data and uncover hidden structure–performance relationships, has become a central tool for the rational design of propane dehydrogenation (PDH) catalysts. By integrating density functional theory (DFT) datasets with experimental measurements, ML enables rapid prediction and optimization of catalytic activity, selectivity, and stability, substantially reducing the cost associated with traditional trial-and-error approaches.

Drawing on recent studies of catalyst systems such as single-atom alloys (SAAs) and multicomponent metal oxides, this section provides a systematic overview of ML applications in catalyst screening, compositional optimization, and mechanistic interpretation.

4.3.1 Dataset Construction and Feature Engineering

High-quality datasets and rational feature selection are fundamental for accurate ML model predictions. Datasets typically originate from DFT calculations or experimental measurements, while features must encompass atomic structure, electronic properties, and reaction characteristics. Data source and scale: 92 C-H bond cleavage barriers on 23 SAA surfaces were calculated via DFT to construct the core dataset. To expand prediction scope, the model was further applied to predict 212 C-H bond barriers for 53 SAAs (M_1M_host, M=Ni, Ru and 6 other active metals; M_host=Al, Fe and 9 other host metals).[11] Datasets were constructed from 200 experimental data points covering 100 multi-component metal oxide catalysts (including propane conversion, propylene yield, CO_2 conversion, and other indicators), with reaction conditions including calcination temperature, reaction temperature, CO_2 flow rate, and other key variables.[5]

Feature selection and optimization: Feature engineering must balance correlation and redundancy, screening core parameters that accurately describe catalytic performance. From 23 initial features (atomic radius, lattice constant, surface energy, electron affinity, etc.), 12 optimal features were selected, including lattice constant, surface energy, atomic radius, and work function of active metals; atomic number, group number, and atomic mass of host metals; and dehydrogenation reaction steps. Dehydrogenation steps showed the most significant impact on C-H bond activation barriers (feature importance ratio 0.65). [11] Fifteen catalyst composition features (metal/support molar ratios) and 3 experimental condition features (calcination temperature, reaction temperature, CO_2 flow rate) were selected as inputs. Pearson correlation analysis revealed that Cr content, ZrO_2 content, and reaction temperature are key factors affecting propylene yield (correlation coefficients 0.39, 0.36, and 0.34, respectively) [Fig. 12(b)-(c)]. [5]

4.3.2 Machine Learning Model Construction and Performance Validation

To meet PDH catalyst prediction requirements, highly adaptable ML algorithms must be selected, with cross-validation ensuring model generalization capability. Model selection and optimization: Eight ML algorithms were compared (polynomial linear regression, random forest, gradient boosting regression, ensemble regression, etc.). The ensemble regression (BAR) model performed optimally, achieving R^2=0.98 and RMSE of only 0.06 eV for C-H bond barrier predictions, far superior to other algorithms (e.g., random forest R^2=0.78).[11] Gradient boosting decision tree (GBDT) models were employed, with hyperparameters optimized through five-fold cross-validation. The final model achieved R^2=0.80 and MAE=0.012 for propylene yield prediction, and R^2=0.82 and MAE=0.011 for predicting the geometric mean of "propylene yield × CO_2 conversion" (Score), accurately capturing nonlinear structure-performance relationships of multi-component catalysts.[5]

Model validation methods: To avoid overfitting, leave-one-out cross-validation (LOOCV) and training-test set splitting (e.g., 8:2 ratio) are typically used to validate model stability [Fig. 12(d)-(e)]. GBDT models were validated through LOOCV, ensuring each data point is fully trained by remaining data. Through 500 repeated training runs and adding random noise, BAR model robustness was verified, with RMSE fluctuations less than 0.01 eV, demonstrating reliable prediction capability. [11]

4.3.3 Rapid Catalyst Screening and Performance Prediction

ML models can efficiently screen massive candidate catalysts, rapidly identify high-performance systems and significantly improve R&D efficiency.

Single-Atom Alloy Catalyst Screening: Using the trained BAR model to predict C-H bond activation barriers for 53 SAAs, $Ru_1Cu(111)$ SAA was found to perform optimally: its first-step propane dehydrogenation barrier is only 0.36 eV, lower than the traditional Pt(111) surface (0.55 eV); the propylene deep dehydrogenation barrier (1.00 eV) is higher than Pt(111) (0.79 eV), and the C-C bond cleavage barrier (1.65 eV) is significantly higher than Pt(111), demonstrating excellent propylene selectivity and anti-coking capability.[11] DFT validation and microkinetic simulations further confirmed that $Ru_1Cu(111)$ also exhibits superior activity compared to Pt in ethane and isobutane dehydrogenation, with its d-band center closer to the Fermi level, enhancing alkane adsorption and C-H bond activation ability.

Multi-Component Metal Oxide Screening: For CO_2-assisted PDH reactions, ML models screened multi-component metal oxide catalysts, finding the Cr-Ni-Co-ZrO_x system to perform optimally.[5] In this catalyst, Cr serves as the active center, while Ni and Co introduction can increase the Cr^{6+}/Cr^{3+} ratio (from 0.66 to 1.13), enhancing C-H bond activation capability; simultaneously, Ni and Co promote CO_2 dissociation, removing H_2 through the reverse water-gas shift reaction, pushing the equilibrium toward propylene formation. DFT calculations confirmed that Ni/Co doping makes surface oxygen species more electrophilic, reducing oxygen vacancy formation energy (from 2.76 eV to 1.88 eV), improving CO_2 conversion activity [Fig. 12(h)].

4.3.4 Closed-Loop Optimization and Structure-Activity Relationship Analysis

The core advantage of ML lies in revealing catalytic performance regulation mechanisms through iterative optimization and feature importance analysis, guiding precise catalyst design.

Closed-Loop Optimization Strategy: A closed-loop optimization framework of "ML model training → catalyst design → experimental validation → data feedback" was proposed.[5] Using the Artificial Bee Colony (ABC) algorithm as the optimizer and based on GBDT model predictions, after 4 iterations, the optimal catalyst $Cr_{7.0}Ni_{1.7}Co_{0.5}$-ZrO_x was obtained, with propylene yield (26%) and CO_2 conversion (29%) significantly higher than the best single-component $Cr_{8.0}$-ZrO_x catalyst in the initial database (propylene yield 21 %, CO_2 conversion 22 %) [Fig. 12(a),(f)-(g)]. After each optimization round, new experimental data was added to the database and the model retrained, continuously improving prediction accuracy.

Structure-Activity Relationship Analysis: Through feature importance analysis, key factors and intrinsic mechanisms affecting catalytic performance can be clarified. The surface energy of active metals is a core factor affecting C-H bond activation, with a negative correlation between them (when surface energy exceeds 2.3 $J \cdot m^{-2}$, the barrier stabilizes) ; the high importance of dehydrogenation steps indicates that the unsaturation degree of carbon species directly determines C-H bond activation difficulty, providing theoretical basis for balancing activity and selectivity. Through XPS and DFT combination, the Ni/Co promotion mechanism was revealed: electron transfer between Ni/Co and Cr increases Cr^{6+} species while reducing surface oxygen Bader charge (from 6.95 e to 6.31 e), enhancing C-H bond activation capability and CO_2 dissociation activity. [5]

4.3.5 Methodological Advantages and Application Prospects

Advantages and Innovations: ML breaks through the system scale limitations of DFT calculations, completing screening of thousands of candidate catalysts within hours, whereas traditional DFT calculations require months; simultaneously, ML can mine nonlinear structure-activity relationships, such as the "active metal surface energy - C-H bond barrier" correlation,[11] and multi-metal synergistic effects, which are difficult to obtain through traditional theoretical analysis.[5]

Future Directions: Current ML models still depend on high-quality datasets. Future work needs to expand data scale and diversity, integrating in-situ characterization data to improve model adaptability to

real reaction conditions; meanwhile, interpretable ML models (such as SHAP, LIME algorithms) need to be developed to reduce "black box" prediction limitations; additionally, combining multi-scale simulations (DFT+ML+microkinetics) can achieve full-chain predictions from atomic structure to macroscopic performance, providing more comprehensive theoretical guidance for industrial application of PDH catalysts.

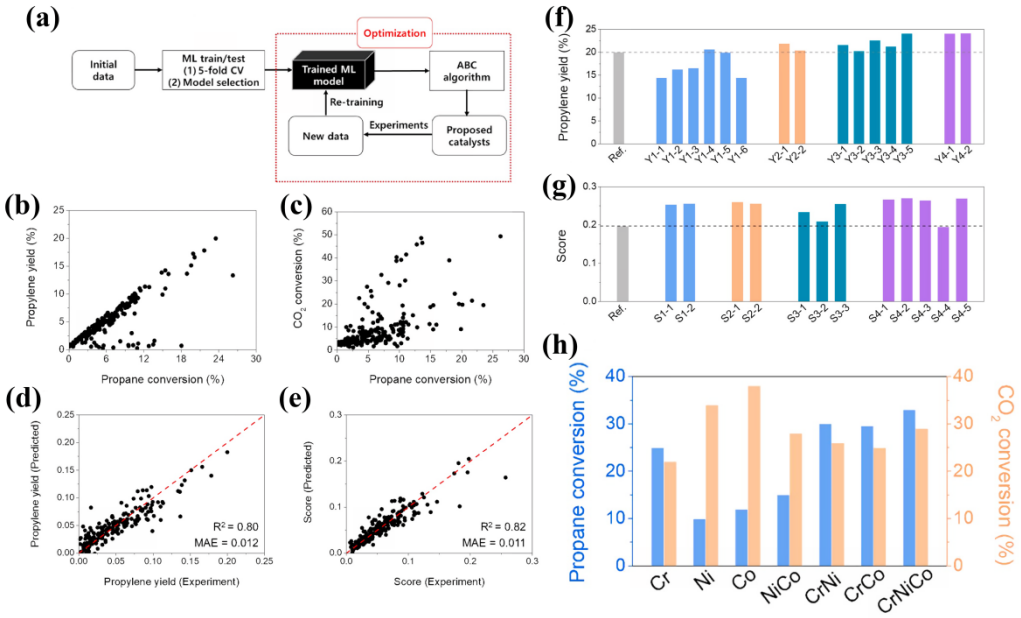

Figure 12. Schematics of (a) data representation and (b) closed-loop optimization process. Here, "Calcin_temp", "Rxn_temp", and "Flow_CO_2" mean calcination temperature, reaction temperature, and flow rate of CO_2, respectively. Distribution of the in-house experimental database for the (b) propylene yield and (c) CO_2 conversion by the propane conversion. Leave-one-out cross-validation results of GBDT model for (d) propylene yield and (e) score. Red dashed line indicates an ideal model. (f) Propylene yield and (g) score of the proposed catalysts throughout the closed-loop optimization process. Here, "Y" and "S" indicate the propylene yield and score, respectively. For example, "Y1–1" denotes the first catalyst proposed in the first cycle of the optimization. "Ref." indicates the Cr8.0-ZrOx catalyst in the initial dataset. (Reaction condition: 600 ◦C, C_3H_8:CO_2 = 1:1, WHSVC_3H_8 = 7.2 h-1).(h) Propane and CO_2 conversion(Reaction condition: 600 ◦C, C_3H_8:CO_2= 1:1, WHSV C_3H_8 = 7.2 h–1)

4.4 High-Throughput Computing and Structure Descriptor Development

High-throughput computing leverages automated workflows to achieve rapid screening of massive candidate catalyst systems, while structure descriptors, as the core bridge connecting catalyst microstructure with macroscopic performance, provide critical basis for accurate prediction of catalytic activity, selectivity, and stability. Their combination greatly shortens the R&D cycle for propane dehydrogenation (PDH) catalysts, promoting the transition from "trial-and-error" to "rational design."

4.4.1 Screening Workflows and Application Scenarios for High-Throughput Computing

High-throughput computing achieves efficient evaluation of large-scale candidate catalysts through automated "structure generation - property calculation - performance screening" workflows, with core advantages in rapidly traversing chemical space and identifying promising systems.

High-Throughput Screening of Alloy Catalysts: For Cu-based alloy catalysts, 1500 Cu_3M_1 (M covering 3d, 4d, 5d metals and main group elements like Al, Ga) candidate structures were constructed,

completing stability and catalytic performance evaluation through density functional theory (DFT) high-throughput calculations. [73] The screening process consisted of three steps: first, thermodynamically stable alloys were screened by formation energy (formation energy < 0.20 eV), yielding 46 surface structures; then, easily reconstructed systems were excluded through surface energy analysis, retaining 38 effective surfaces; finally, combining key PDH reaction performance indicators, four high-performance catalysts Cu_3Cr_1, Cu_3Pd_1, Cu_3Pt_1, and Cu_3Ag_1 were screened [Fig. 13(a)]. [74] This workflow efficiently traversed the chemical space of Cu-based alloys, clarifying the mechanism of alloying on Cu catalytic activity enhancement.

High-Throughput Evaluation of Single-Atom Catalysts: For graphene-supported single Pt atom catalysts, 12 different doping configurations (pure N doping, pure B doping, and N-B co-doping) were designed, systematically studying the effects of doping type and ratio on Pt electronic structure and PDH performance through high-throughput DFT calculations. [75] Results showed that pyridinic N doping (3NG configuration) optimally adjusted Pt's d-band center, reducing propane C-H bond activation barrier to 0.37 eV, significantly outperforming pure graphene and B-doped systems, providing clear direction for support engineering of single-atom catalysts [Fig. 13(c)].

4.4.2 Development and Classification of Core Structure Descriptors

Structure descriptors must have clear physical meaning and strong correlation with catalytic performance. They can be classified into three categories: electronic structure descriptors, geometric structure descriptors, and reaction kinetics descriptors, collectively forming core indicators for catalyst performance prediction.

Electronic Structure Descriptors:

d-Band Center: As a classic descriptor for transition metal catalysts, it reflects the interaction strength between metal surfaces and adsorbates. N doping shifts Pt's d-band center toward the Fermi level (d-band center at -2.0 eV in 3NG configuration vs. -2.5 eV on pure graphene support), enhancing Pt-propane interaction and reducing C-H bond activation barrier; while B doping moves the d-band center away from the Fermi level, reducing catalytic activity. [75] Further confirmation showed that Ru's d-band center in $Ru_1Cu(111)$ SAA is closer to the Fermi level, with C-H bond activation barrier (0.36 eV) lower than traditional Pt(111) surface (0.55 eV).

Charge State: The charge distribution of catalyst active sites directly affects electron transfer efficiency. [11] Bader charge analysis shows that N doping makes Pt positively charged (Pt charge +0.8 e in 3NG configuration), enhancing polarization capability for propane C-H bonds; while B doping makes Pt negatively charged (Pt charge -0.6 e in 3BG configuration), weakening C-H bond activation capability. Charge state linearly correlates with C-H bond activation barrier ($R^2 = 0.68$) [Fig. 13(e)]. [75]

Geometric Structure Descriptors:

Surface Coordination Number: The coordination number of active sites directly affects catalytic activity. Low-coordination surface sites in single-atom alloys (SAA) (such as (211) steps, (100)-(110) interfaces) have lower coordination numbers than (111) terrace sites, with significantly reduced C-H bond activation barriers. In Rh-Cu SAA, (111) adatom sites exhibit 100 times higher reactivity than (111) terrace sites. [72] The coordination number of Pd atoms on Cu_3Pd_1 alloy surface (4) is lower than that of Pd atoms on pure Pd(111) surface (9), making Pd's electronic structure easier to modulate, optimizing the balance between C-H bond activation and propylene desorption.

Bond Length and Lattice Constants: Lattice distortion in alloys modulates active site electronic structure. Lattice constants regulate catalytic performance by affecting C-H-M interaction strength; smaller lattice constants bring C-H bonds closer to the metal surface, enhancing agostic interactions and promoting C-H bond activation; Ru_1Cu alloy's lattice constant (3.61 Å) lies between Ru (3.80 Å) and Cu (3.61 Å), moderately adjusting Ru atom electronic structure, balancing propane adsorption and propylene desorption.[11]

Reaction Kinetics Descriptors:

C-H Bond Activation Barrier: As a descriptor for the rate-determining step of PDH reactions, it directly reflects catalyst activity. Using this as a core screening indicator, Cu_3Cr_1's C-H bond activation barrier (0.83 eV) is significantly lower than pure Cu(111) surface (1.31 eV), becoming a key basis for screening. [73]

Propylene Desorption Energy and Deep Dehydrogenation Energy Difference (Ediff): Used to evaluate catalyst selectivity, Ediff = Edeep - $E_{des}C_3H_6$ (Edeep is propylene deep dehydrogenation barrier, $E_{des}C_3H_6$ is propylene desorption energy); positive values indicate propylene more readily desorbs than undergoes deep dehydrogenation. The Ediff of Cu2Ag1 is 0.23 eV, while Ediff of pure Cu (111) is -0.17 eV, indicating alloying significantly improves propylene selectivity [Fig. 13(b),(d)]. [74]

Oxygen Vacancy Formation Energy: For metal oxide catalysts in CO_2-assisted PDH reactions, oxygen vacancies are key sites for CO_2 activation. Ni/Co doping reduces ZrO_2 oxygen vacancy formation energy from 2.76 eV to 1.88 eV, enhancing CO_2 dissociation capability, removing H_2 through reverse water-gas shift reactions, and driving PDH equilibrium forward. [5]

4.4.3 Descriptor Scaling Relations and Application Extensions

Scaling relations establish linear correlations between different descriptors or performance indicators, further simplifying catalyst screening workflows and improving prediction efficiency, serving as an important supplement to high-throughput computing.

Scaling Relations Between Descriptors: Site-specific scaling relations based on methyl adsorption energy were established; methyl adsorption energy at top sites can predict adsorption energies of other C_1 species (CH, CH_2, C) at tetrahedral coordination sites, with mean absolute error (MAE) as low as 0.11 eV [Fig. 13(f)-(g)]. [76] Combined with gas-phase C-H bond energies, this relation can further predict adsorption energies of long-chain hydrocarbons (such as propyl, propargyl), enabling rapid evaluation of PDH reaction networks. C-H bond dissociation energy and reaction barrier follow the Brønsted-Evans-Polanyi (BEP) relationship (R^2 = 0.94), allowing rapid prediction of kinetic performance through thermodynamic descriptors [Fig. 13(h)]. [75]

Application of Descriptors in Multi-Component Catalysts: Descriptor-performance correlations were established through Pearson correlation analysis, finding Cr content (correlation coefficient 0.39), ZrO_2 content (0.36), and reaction temperature (0.34) as key descriptors affecting propylene yield, providing clear direction for component optimization of multi-component metal oxide catalysts. [5] Inputting 12 descriptors (active metal surface energy, host metal atomic number, etc.) into machine learning models successfully predicted C-H bond activation barriers for 53 SAAs, screening out high-performance catalysts like Ru_1Cu, validating descriptor effectiveness in large-scale screening. [11]

4.4.4 Methodological Advantages and Future Directions

Advantages and Innovations: The combination of high-throughput computing and structure descriptors achieves an integrated R&D model of "massive screening - precise positioning - mechanism analysis." For example, through four-step descriptor screening (formation energy → surface energy → propylene desorption energy → C-H activation barrier), 4 high-performance Cu-based alloys were rapidly identified from 1500 candidate systems, with efficiency improved by two orders of magnitude compared to traditional experiments;[73] the physical clarity of descriptors makes screening results interpretable, with descriptors like d-band center and coordination number directly correlating with microscopic origins of catalytic performance.

Future Directions: Current descriptors remain primarily single-dimensional; future work needs to develop multi-dimensional coupled descriptors comprehensively considering synergistic effects of electronic structure, geometric structure, and reaction environment; high-throughput computing needs to extend to more complex real reaction conditions (such as high temperature, high pressure, reactant/product atmospheres) to improve screening result practicality; additionally, combining machine learning to construct nonlinear prediction models for descriptor-performance relationships can further break through

linear scaling relation limitations, achieving more precise catalyst performance prediction and providing more powerful tools for rational design of PDH catalysts.

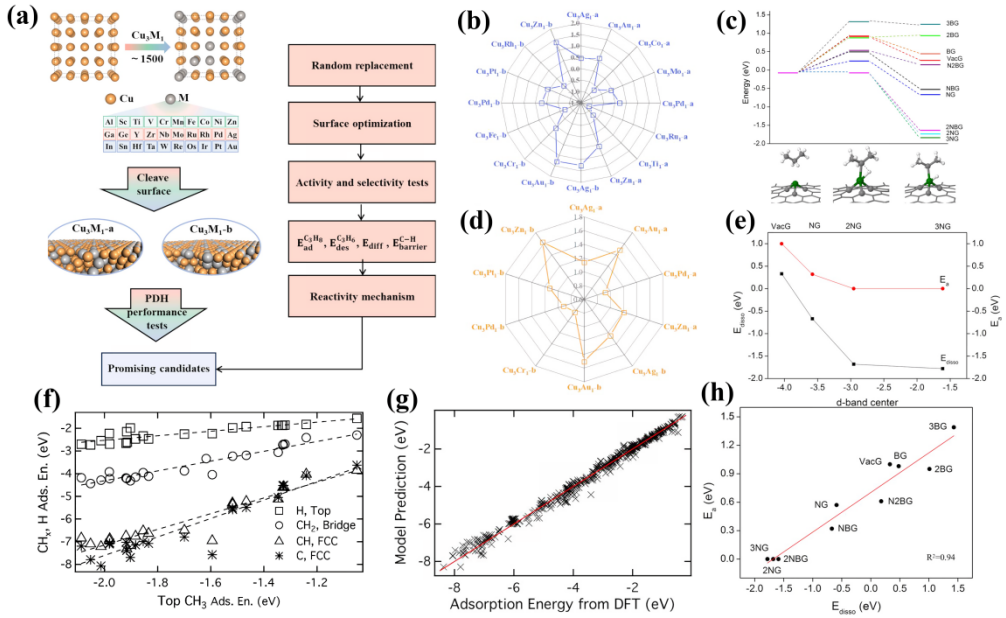

Figure 13. (a) Workflow of high-throughput computational screening of Cu-based alloy catalysts for PDH. (b) Ediff varies with the different alloy surfaces, (c) Reaction pathway of the first C−H bond breaking in propane molecule on the supported single Pt catalyst. The important structures along the pathway are also shown at the bottom (initial, transition, final states from left to right). (d) EBarrier C− H varies with the different alloy surfaces (e) Relation between the d-band center of single Pt atom on various supports with the dissociation energy and reaction barrier. (f) Site-specific scaling relations, with each C1 adsorbate in its tetravalent site and H in its divalent site. (g) Parity plot for eqs 8−15 applied to the 527-point data set. (h) Linear relation between the calculated dissociation energy and barrier for the activation of the first C−H bond.

References

[1] Lin, J.; Shen, M.; Zhang, C.; Bi, S.; Shen, G.; Gao, F.; Li, W. Active and stable platinum-indium single atom alloy catalysts for propane dehydrogenation. *Chemical Engineering Journal* **2025**, *519*. DOI: 10.1016/j.cej.2025.165243.

[2] Liu, M.; Han, S.; Zhang, W.; Gu, B.; Li, J.; Wei, H.; Rong, X.; Sun, C. Boron-Induced Redispersion of Pt Species during Propane Dehydrogenation. *ACS Catalysis* **2025**, *15* (5), 4251-4258. DOI: 10.1021/acscatal.4c07243.

[3] Lin, J.; Shen, M.; Bi, S.; Shen, G.; Gao, F.; Li, W. PtIn Alloy Supported on Y2O3-Modified δ-Al2O3 as a Propane Dehydrogenation Catalyst. *ACS Catalysis* **2025**, *15* (14), 12407-12419. DOI: 10.1021/acscatal.5c03103.

[4] Wang, S.-W.; He, Z.-H.; Tian, Y.; Zhu, Z.-J.; Sun, Y.-C.; Wang, K.; Wang, W.; Yang, Y.; Wang, H.; Liu, Z.-T. Photothermal catalytic CO2 oxidative dehydrogenation of propane over a dual functional Pt-GaN/SrTiO3 catalyst. *Applied Catalysis B: Environment and Energy* **2024**, *356*. DOI: 10.1016/j.apcatb.2024.124246.

[5] Kim, J.-S.; Chung, I.; Oh, J.; Park, J.; Yun, Y.; Shin, J.; Kim, H. W.; Chang, H. Closed-loop optimization of catalysts for oxidative propane dehydrogenation with CO2 using artificial intelligence. *Journal of CO2 Utilization* **2023**, *78*. DOI: 10.1016/j.jcou.2023.102620.

[6] Wang, Z.; Chen, H.; Song, S.; Liu, B.; Song, W.; Li, L.; Liu, J. Hydroxyl-Poor Al2O3 Avoids the Formation of ZnAl2O4 Spinel for Propane Dehydrogenation. *Industrial & Engineering Chemistry Research* **2024**, *63* (45), 19457-19465. DOI: 10.1021/acs.iecr.4c02389.

[7] Hao, X.; Zhao, X.; Zhou, Y.; Xu, Y.; Xia, J.; Wu, L.; Wei, T.; He, Z.-H.; Ma, S.; Xu, B. Boosting photothermal propane dehydrogenation via synergistic Co-Zr doping in CeO2 nanorods. *Molecular Catalysis* **2026**, *590*. DOI: 10.1016/j.mcat.2025.115634.

[8] Liu, X.; Yao, Z.; Lai, J.; Li, J.; Wang, J. Hydrogen coverage effects and structure sensitivity in propane dehydrogenation on Pt nanoparticles. *Chemical Engineering Science* **2026**, *319*. DOI: 10.1016/j.ces.2025.122299.

[9] Sun, S.; Sun, G.; Pei, C.; Zhao, Z.-J.; Gong, J. Origin of Performances of Pt/Cu Single-Atom Alloy Catalysts for Propane Dehydrogenation. *The Journal of Physical Chemistry C* **2021**, *125* (34), 18708-18716. DOI: 10.1021/acs.jpcc.1c04295.

[10] Xu, S.; Huang, Y.; Qie, M.; Yang, Y.; Wang, W.; Wu, K.; Li, W.; Li, Z.; Shen, Z.; Yang, H. Density functional theory study on propane dehydrogenation to propylene catalyzed by β-Mo2C(001)-based catalysts. *International Journal of Hydrogen Energy* **2025**, *179*. DOI: 10.1016/j.ijhydene.2025.151711.

[11] Feng, H.; Ge, Z.; Deng, Y.; Pu, P.; Zhao, S.; Song, X.; Yuan, H.; Wu, Y.; Yang, J.; Si, Y.; et al. Unveiling high-performance single-atom alloy catalysts for alkane dehydrogenation through DFT and machine learning synergy. *Journal of Catalysis* **2025**, *448*. DOI: 10.1016/j.jcat.2025.116213.

[12] Liang, K.; Zeng, X.; Ma, R.; Zou, G.; Dang, L.; Li, S. A theoretical investigation of propane dehydrogenation on Pt and Ni-based alloys. *Journal of Catalysis* **2023**, *428*. DOI: 10.1016/j.jcat.2023.115162.

[13] Cao, L.; Wei, F.; Chen, Y.; Pan, X.; Cao, H.; Su, Y.; Zhao, Y.; Chen, D.; Chai, Y.; Chen, L.; et al. Atomic Coordination Editing Achieves Ultraproductive Single-Atom Catalysts with Ultralow Loadings. *Journal of the American Chemical Society* **2025**, *147* (42), 38752-38761. DOI: 10.1021/jacs.5c14188.

[14] Salom-Català, A.; Strugovshchikov, E.; Kaźmierczak, K.; Curulla-Ferré, D.; Ricart, J. M.; Carbó, J. J. Reactive Force Field Development for Propane Dehydrogenation on Platinum Surfaces. *The Journal of Physical Chemistry C* **2024**, *128* (7), 2844-2855. DOI: 10.1021/acs.jpcc.3c07126.

[15] Liu, Z.; Lu, A.-H.; Wang, D. Deep Potential Molecular Dynamics Study of Propane Oxidative Dehydrogenation. *The Journal of Physical Chemistry A* **2024**, *128* (9), 1656-1664. DOI: 10.1021/acs.jpca.3c07859.

[16] Xiao, L.; Shan, Y.-L.; Sui, Z.-J.; Chen, D.; Zhou, X.-G.; Yuan, W.-K.; Zhu, Y.-A. Beyond the Reverse Horiuti–Polanyi Mechanism in Propane Dehydrogenation over Pt Catalysts. *ACS Catalysis* **2020**, *10* (24), 14887-14902. DOI: 10.1021/acscatal.0c03381.

[17] Pan, J.; Bru, G.; Carbó, J. J.; Godard, C.; Ricart, J. M. Propane Dehydrogenation Catalyzed by Pt Clusters (Pt2–Pt6) in Gas Phase and Supported on g-C3N4 and γ-Al2O3: A Theoretical Study. *ACS Omega* **2025**, *10* (39), 46105-46114. DOI: 10.1021/acsomega.5c07626.

[18] Fricke, C.; Rajbanshi, B.; Walker, E. A.; Terejanu, G.; Heyden, A. Propane Dehydrogenation on Platinum Catalysts: Identifying the Active Sites through Bayesian Analysis. *ACS Catalysis* **2022**, *12* (4), 2487-2498. DOI: 10.1021/acscatal.1c04844.

[19] Zhu, J.; Yang, M.-L.; Yu, Y.; Zhu, Y.-A.; Sui, Z.-J.; Zhou, X.-G.; Holmen, A.; Chen, D. Size-Dependent Reaction Mechanism and Kinetics for Propane Dehydrogenation over Pt Catalysts. *ACS Catalysis* **2015**, *5* (11), 6310-6319. DOI: 10.1021/acscatal.5b01423.

[20] Nykänen, L.; Honkala, K. Density Functional Theory Study on Propane and Propene Adsorption on Pt(111) and PtSn Alloy Surfaces. *The Journal of Physical Chemistry C* **2011**, *115* (19), 9578-9586. DOI: 10.1021/jp1121799.

[21] Wang, J.; Chang, X.; Chen, S.; Sun, G.; Zhou, X.; Vovk, E.; Yang, Y.; Deng, W.; Zhao, Z.-J.; Mu, R.; et al. On the Role of Sn Segregation of Pt-Sn Catalysts for Propane Dehydrogenation. *ACS Catalysis* **2021**, *11* (8), 4401-4410. DOI: 10.1021/acscatal.1c00639.

[22] Yang, M.-L.; Zhu, Y.-A.; Zhou, X.-G.; Sui, Z.-J.; Chen, D. First-Principles Calculations of Propane Dehydrogenation over PtSn Catalysts. *ACS Catalysis* **2012**, *2* (6), 1247-1258. DOI: 10.1021/cs300031d.

[23] Pan, J.; Strugovshchikov, E.; Salóm-Català, A.; Novell-Leruth, G.; Kaźmierczak, K.; Curulla-Ferré, D.; Carbó, J. J.; Godard, C.; Ricart, J. M. Propane Dehydrogenation on Pt Single-Atom and Pt4 and Pt3Sn Single-Cluster Supported on g-C3N4: A Theoretical Study. *The Journal of Physical Chemistry C* **2025**, *129* (5), 2477-2487. DOI: 10.1021/acs.jpcc.4c07686.

[24] Liu, Y.; Zong, X.; Patra, A.; Caratzoulas, S.; Vlachos, D. G. Propane Dehydrogenation on PtxSny (x, y ≤ 4) Clusters on Al2O3(110). *ACS Catalysis* **2023**, *13* (5), 2802-2812. DOI: 10.1021/acscatal.2c05671.

[25] Fricke, C. H.; Bamidele, O. H.; Bello, M.; Chowdhury, J.; Terejanu, G.; Heyden, A. Modeling the Effect of Surface Platinum–Tin Alloys on Propane Dehydrogenation on Platinum–Tin Catalysts. *ACS Catalysis* **2023**, *13* (16), 10627-10640. DOI: 10.1021/acscatal.3c00939.

[26] Liu, D.; Jiang, F.; Zhang, Q.; Huang, W.-H.; Zheng, Y.; Chen, M.; Wu, L.; Qin, R.; Wang, M.; Zhang, S.; et al. Pt–ZnOx Interfacial Effect on the Performance of Propane Dehydrogenation and Mechanism Study. *ACS Nano* **2024**, *18* (51), 34671-34682. DOI: 10.1021/acsnano.4c10030.

[27] Rochlitz, L.; Fischer, J. W. A.; Pessemesse, Q.; Clark, A. H.; Ashuiev, A.; Klose, D.; Payard, P.-A.; Jeschke, G.; Copéret, C. Ti-Doping in Silica-Supported PtZn Propane Dehydrogenation Catalysts: From Improved Stability to the Nature of the Pt–Ti Interaction. *JACS Au* **2023**, *3* (7), 1939-1951. DOI: 10.1021/jacsau.3c00197.

[28] Yang, M.-L.; Fan, C.; Zhu, Y.-A.; Sui, Z.-J.; Zhou, X.-G.; Chen, D. Selective Oxidation of Hydrogen in the Presence of Propylene over Pt-Based Core–Shell Nanocatalysts. *The Journal of Physical Chemistry C* **2015**, *119* (37), 21386-21394. DOI: 10.1021/acs.jpcc.5b03733.

[29] Chang, Q.-Y.; Yin, Q.; Ma, F.; Zhu, Y.-A.; Sui, Z.-J.; Zhou, X.-G.; Chen, D.; Yuan, W.-K. Tuning Adsorption and Catalytic Properties of α-Cr2O3 and ZnO in Propane Dehydrogenation by Creating Oxygen Vacancy and Doping Single Pt Atom: A Comparative First-Principles Study. *Industrial & Engineering Chemistry Research* **2019**, *58* (24), 10199-10209. DOI: 10.1021/acs.iecr.9b01143.

[30] Conley, M. P.; Delley, M. F.; Núñez-Zarur, F.; Comas-Vives, A.; Copéret, C. Heterolytic Activation of C–H Bonds on CrIII–O Surface Sites Is a Key Step in Catalytic Polymerization of Ethylene and Dehydrogenation of Propane. *Inorganic Chemistry* **2015**, *54* (11), 5065-5078. DOI: 10.1021/ic502696n.

[31] Huš, M.; Kopač, D.; Bajec, D.; Likozar, B. Effect of Surface Oxidation on Oxidative Propane Dehydrogenation over Chromia: An Ab Initio Multiscale Kinetic Study. *ACS Catalysis* **2021**, *11* (17), 11233-11247. DOI: 10.1021/acscatal.1c01814.

[32] Jin, D.; Xu, H.; Zhu, J.; Cheng, D. Activation of Cr2O3 for propane dehydrogenation by doping with Pt single-atom promotor. *Molecular Catalysis* **2023**, *551*. DOI: 10.1016/j.mcat.2023.113624.

[33] Li, R.; Zhang, C.; Li, S.; Du, Y. Experimental and theoretical investigations into propane dehydrogenation over MIL-101(Cr/Al) derived catalysts. *Molecular Catalysis* **2023**, *535*. DOI: 10.1016/j.mcat.2022.112894.

[34] Han, S.; Zhao, Y.; Otroshchenko, T.; Zhang, Y.; Zhao, D.; Lund, H.; Vuong, T. H.; Rabeah, J.; Bentrup, U.; Kondratenko, V. A.; et al. Unraveling the Origins of the Synergy Effect between ZrO2 and CrOx in Supported CrZrOx for Propene Formation in Nonoxidative Propane Dehydrogenation. *ACS Catalysis* **2019**, *10* (2), 1575-1590. DOI: 10.1021/acscatal.9b05063.

[35] Dai, G.-L.; Li, Z.-H.; Lu, J.; Wang, W.-N.; Fan, K.-N. Deep Oxidations in the Oxidative Dehydrogenation Reaction of Propane over V2O5(001): Periodic Density Functional Theory Study. *The Journal of Physical Chemistry C* **2011**, *116* (1), 807-817. DOI: 10.1021/jp208639t.

[36] Huang, C.; Wang, Z.-Q.; Gong, X.-Q. Activity and selectivity of propane oxidative dehydrogenation over VO 3 /CeO 2 (111) catalysts: A density functional theory study. *Chinese Journal of Catalysis* **2018**, *39* (9), 1520-1526. DOI: 10.1016/s1872-2067(18)63072-4.

[37] Mokhtari, Z.; Towfighi Darian, J.; Safari Yazd, M. Mechanistic elucidation of MgO-doped VOx@ZrO2 catalysts for enhanced CO2-assisted oxidative dehydrogenation of propane: Tuning oxygen vacancies, spillover, and redox–base properties. *International Journal of Hydrogen Energy* **2025**, *183*. DOI: 10.1016/j.ijhydene.2025.151854.

[38] Liu, Y.; Zhang, T.; Yang, J.; Dong, J.; Fu, Z.; Chu, C.; He, Y.; Bing, L.; Lan, X.; Li, J.; et al. Design and experimental synthesis of VOx/SSZ-13 catalyst based on first principles calculations - elucidating the role of VOx microstructure and valence state in propane dehydrogenation. *Journal of Environmental Chemical Engineering* **2026**, *14* (1). DOI: 10.1016/j.jece.2025.120954.

[39] Shan, Y.-L.; Sun, H.-L.; Zhao, S.-L.; Tang, P.-L.; Zhao, W.-T.; Ding, J.-W.; Yu, W.-L.; Li, L.-N.; Feng, X.; Chen, D. Effects of Support and CO2 on the Performances of Vanadium Oxide-Based Catalysts in Propane Dehydrogenation. *ACS Catalysis* **2022**, *12* (10), 5736-5749. DOI: 10.1021/acscatal.2c00878.

[40] Arinaga, A. M.; Biswas, A.; Zhang, X.; Greeley, J.; Marks, T. J. Origin of Rate and Selectivity Trends and Exceptional Yield in Sulfur-Oxidative Propane Dehydrogenation Over Supported Vanadium Catalysts. *ACS Catalysis* **2023**, *13* (20), 13395-13413. DOI: 10.1021/acscatal.3c03677.

[41] Chen, H.; Gao, P.; Liu, Z.; Liang, L.; Han, Q.; Wang, Z.; Chen, K.; Zhao, Z.; Guo, M.; Liu, X.; et al. Direct Detection of Reactive Gallium-Hydride Species on the Ga2O3 Surface via Solid-State NMR Spectroscopy. *Journal of the American Chemical Society* **2022**, *144* (38), 17365-17375. DOI: 10.1021/jacs.2c01005.

[42] Yuan, Y.; Lee, J. S.; Lobo, R. F. Ga+-Chabazite Zeolite: A Highly Selective Catalyst for Nonoxidative Propane Dehydrogenation. *Journal of the American Chemical Society* **2022**, *144* (33), 15079-15092. DOI: 10.1021/jacs.2c03941.

[43] Bauer, T.; Maisel, S.; Blaumeiser, D.; Vecchietti, J.; Taccardi, N.; Wasserscheid, P.; Bonivardi, A.; Görling, A.; Libuda, J. Operando DRIFTS and DFT Study of Propane Dehydrogenation over Solid- and Liquid-Supported GaxPty Catalysts. *ACS Catalysis* **2019**, *9* (4), 2842-2853. DOI: 10.1021/acscatal.8b04578.

[44] Madubuko, N.; Hsieh, T.-E.; Vorlaufer, N.; Carl, S.; Steffen, J.; Mölkner, A.; Taccardi, N.; Frisch, J.; Wilks, R. G.; Will, J.; et al. Reductive Treatment of Ga–Pt-Supported Catalytically Active Liquid Metal Solutions (SCALMS) for Propane Dehydrogenation. *ACS Catalysis* **2025**, *15* (14), 12436-12449. DOI: 10.1021/acscatal.5c01463.

[45] Raman, N.; Maisel, S.; Grabau, M.; Taccardi, N.; Debuschewitz, J.; Wolf, M.; Wittkämper, H.; Bauer, T.; Wu, M.; Haumann, M.; et al. Highly Effective Propane Dehydrogenation Using Ga–Rh Supported Catalytically Active Liquid Metal Solutions. *ACS Catalysis* **2019**, *9* (10), 9499-9507. DOI: 10.1021/acscatal.9b02459.

[46] Ji, J.; Fan, G.; Zheng, L.; Li, F. Confinement of Atomically Dispersed Ptδ+ Sites in Zinc-Incorporated Silicalite-1 Zeolite for Enhanced Propane Dehydrogenation. *ACS Catalysis* **2025**, *15* (7), 5858-5875. DOI: 10.1021/acscatal.4c07883.

[47] Liu, H.; Chu, B.; Chen, T.; Zhou, J.; Dong, L.; Lo, T. W. B.; Li, B.; He, X.; Ji, H. Modulation of the cobalt species state on zincosilicate to maximize propane dehydrogenation to propylene. *Chinese Journal of Catalysis* **2024**, *66*, 168-180. DOI: 10.1016/s1872-2067(24)60133-6.

[48] Qu, Y.; Li, G.; Zhao, T.; Zhang, Z.; Douthwaite, M.; Zhang, J.; Hao, Z. Low-Temperature Direct Dehydrogenation of Propane over Binary Oxide Catalysts: Insights into Geometric Effects and Active Sites. *ACS Sustainable Chemistry & Engineering* **2021**, *9* (38), 12755-12765. DOI: 10.1021/acssuschemeng.1c03074.

[49] Chen, S.; Chai, Y.; Chen, Y.; Wei, F.; Pan, X.; Lin, J.; Lin, S. Peripheral P doping in Zn1/NC single-atom catalyst to enhance propane dehydrogenation reaction. *Chemical Engineering Science* **2024**, *291*. DOI: 10.1016/j.ces.2024.119919.

[50] Liu, Y.; Liu, Z.; Lu, W.-D.; Wang, D.; Lu, A.-H. In Situ Generated Boron Peroxo as Mild Oxidant in Propane Oxidative Dehydrogenation Revealed by Density Functional Theory Study. *The Journal of Physical Chemistry Letters* **2022**, *13* (50), 11729-11735. DOI: 10.1021/acs.jpclett.2c03341.

[51] Zhuang, J.; Qin, T.; Qi, W.; Cao, L.; Yao, Z.; Hu, M.; Bing, L.; Wang, Y.; Deng, K.; Liu, X. Accelerated Crystallization of Zeolites via Solid Boron Free Radicals. *JACS Au* **2025**, *5* (7), 3374-3386. DOI: 10.1021/jacsau.5c00468.

[52] Wang, G.; Hu, A.; Duan, Q.; Cui, L.; Chen, Z.; Huang, Z.; Zhang, X.; Huang, S.; Xie, Z. Hierarchical boroncarbonitride nanosheets as metal-free catalysts for enhanced oxidative dehydrogenation of propane. *Chemical Engineering Science* **2024**, *288*. DOI: 10.1016/j.ces.2024.119848.

[53] Gao, X.; Cai, C.; Tian, S.; Xu, S.; Lin, L.; Shi, J.; Song, C.; Wang, T.; Ma, D.; Yao, S. Performance Descriptor of Subsurface Metal-Promoted Boron Catalysts for Low-Temperature Propane Oxidative Dehydrogenation to Propylene. *Journal of the American Chemical Society* **2024**, *146* (51), 35165-35174. DOI: 10.1021/jacs.4c11506.

[54] Zhang, X.; Ren, B.; Yang, Z.; Chen, H.; Dai, S. Transforming Boron Carbon Nitride: A Carbon-to-Oxygen Switch to Boost Propane Oxidative Dehydrogenation. *ACS Catalysis* **2025**, *15* (11), 9290-9300. DOI: 10.1021/acscatal.5c01353.

[55] Zhou, Q.; Liu, Z.; Zhu, L.; Lu, W.; He, L.; Wang, D. Oxidative Dehydrogenation of Propane on Boron Phosphate: A Computational Mechanistic Study. *The Journal of Physical Chemistry C* **2023**, *127* (27), 12942-12952. DOI: 10.1021/acs.jpcc.3c00838.

[56] Zhu, L.; Liu, Z.; Zhou, Q.; Lu, W.-D.; Wang, D. Propane Oxidative Dehydrogenation on Nanosized Boron Carbide: Effect of Boron Content and Its Oxidation Implicated by DFT Calculations. *The Journal of Physical Chemistry C* **2023**, *127* (13), 6280-6293. DOI: 10.1021/acs.jpcc.2c08586.

[57] Liu, Y.; Liu, Z.; Wang, D.; Lu, A.-H. Suppressing Deep Oxidation by Detached Nano-sized Boron Oxide in Oxidative Dehydrogenation of Propane Revealed by the Density Functional Theory Study. *The Journal of Physical Chemistry C* **2022**, *126* (50), 21263-21271. DOI: 10.1021/acs.jpcc.2c06910.

[58] Chang, X.; Lu, Z.; Luo, R.; Wang, X.; Sun, G.; Fu, D.; Zhao, Z.-J.; Gong, J. Microenvironment engineering of non-noble metal alloy for selective propane dehydrogenation. *Chem* **2025**, *11* (1). DOI: 10.1016/j.chempr.2024.08.017.

[59] Liang, K.; Zeng, X.; Dang, L.; Li, S. Structure Sensitivity Study of Propane Dehydrogenation on Cobalt Catalysts: HCP versus FCC. *The Journal of Physical Chemistry C* **2023**, *127* (37), 18409-18419. DOI: 10.1021/acs.jpcc.3c05358.

[60] Li, C.-F.; Guo, X.; Shang, Q.-H.; Yan, X.; Ren, C.; Lang, W.-Z.; Guo, Y.-J. Defective TiO2 for Propane Dehydrogenation. *Industrial & Engineering Chemistry Research* **2020**, *59* (10), 4377-4387. DOI: 10.1021/acs.iecr.9b06759.

[61] Zhang, Y.; Zhao, Y.; Otroshchenko, T.; Perechodjuk, A.; Kondratenko, V. A.; Bartling, S.; Rodemerck, U.; Linke, D.; Jiao, H.; Jiang, G.; et al. Structure–Activity–Selectivity Relationships in Propane Dehydrogenation over Rh/ZrO2 Catalysts. *ACS Catalysis* **2020**, *10* (11), 6377-6388. DOI: 10.1021/acscatal.0c01455.

[62] Araujo-Lopez, E.; Joos, L.; Vandegehuchte, B. D.; Sharapa, D. I.; Studt, F. Theoretical Investigations of (Oxidative) Dehydrogenation of Propane to Propylene over Palladium Surfaces. *The Journal of Physical Chemistry C* **2020**, *124* (5), 3171-3176. DOI: 10.1021/acs.jpcc.9b11424.

[63] Saelee, T.; Namuangruk, S.; Kungwan, N.; Junkaew, A. Theoretical Insight into Catalytic Propane Dehydrogenation on Ni(111). *The Journal of Physical Chemistry C* **2018**, *122* (26), 14678-14690. DOI: 10.1021/acs.jpcc.8b03939.

[64] Li, Y.; Yang, X. Unveiling the Catalytic Mechanism and Selectivity Control Strategies of Two-Dimensional C3N Materials for Propane Oxidative Dehydrogenation: A DFT Study. *The Journal of Physical Chemistry C* **2025**, *129* (43), 19336-19346. DOI: 10.1021/acs.jpcc.5c03202.

[65] Yu, J.; Xu, Y.; Guliants, V. V. Propane ammoxidation over Mo–V–Te–Nb–O M1 phase: Density functional theory study of propane oxidative dehydrogenation steps. *Catalysis Today* **2014**, *238*, 28-34. DOI: 10.1016/j.cattod.2014.02.053.

[66] Dou, J.; Funderburg, J.; Yang, K.; Liu, J.; Chacko, D.; Zhang, K.; Harvey, A. P.; Haribal, V. P.; Zhou, S. J.; Li, F. CexZr1–xO2-Supported CrOx Catalysts for CO2-Assisted Oxidative Dehydrogenation of Propane─Probing the Active Sites and Strategies for Enhanced Stability. *ACS Catalysis* **2022**, *13* (1), 213-223. DOI: 10.1021/acscatal.2c05286.

[67] Zhai, P.; Xie, Z.; Huang, E.; Aireddy, D. R.; Yu, H.; Cullen, D. A.; Liu, P.; Chen, J. G.; Ding, K. CO2-mediated oxidative dehydrogenation of propane enabled by Pt-based bimetallic catalysts. *Chem* **2023**, *9* (11), 3268-3285. DOI: 10.1016/j.chempr.2023.07.002.

[68] Nie, X.; Zhao, S.; Liu, T.; Qu, S.; Fan, H.; Song, C.; Guo, X. Computational Identification of Catalytic Mechanism and Performance of Pt4/Fe-MFI Catalyst for Propane Dehydrogenation. *Energy & Fuels* **2025**, *39* (37), 18053-18065. DOI: 10.1021/acs.energyfuels.5c02867.

[69] Yang, Y.; Liao, R.; Pu, R.; Jiang, P.; Li, L.; Wang, X.; Ji, H. A new isopropanol-intermediate mechanism for CO2-assisted propane dehydrogenation over ZIF-derived (GaCe)Ox: Toward propylene synthesis. *Chemical Engineering Journal* **2025**, *525*. DOI: 10.1016/j.cej.2025.170285.

[70] Seemakurthi, R. R.; Canning, G.; Wu, Z.; Miller, J. T.; Datye, A. K.; Greeley, J. Identification of a Selectivity Descriptor for Propane Dehydrogenation through Density Functional and Microkinetic Analysis on Pure Pd and Pd Alloys. *ACS Catalysis* **2021**, *11* (15), 9588-9604. DOI: 10.1021/acscatal.1c01916.

[71] Yang, T.; Zhong, Y.; Li, J.; Ma, R.; Yan, H.; Liu, Y.; He, Y.; Li, D. Construction of a Unique Structure of Ru Sites in the RuP Structure for Propane Dehydrogenation. *ACS Applied Materials & Interfaces* **2021**, *13* (28), 33045-33055. DOI: 10.1021/acsami.1c07842.

[72] Bunting, R. J.; Wodaczek, F.; Torabi, T.; Cheng, B. Reactivity of Single-Atom Alloy Nanoparticles: Modeling the Dehydrogenation of Propane. *Journal of the American Chemical Society* **2023**, *145* (27), 14894-14902. DOI: 10.1021/jacs.3c04030.

[73] Wang, X.; Zhao, H.; Ma, Y.; Wang, L.; Li, Y.; Chi, L. Discovery of promising Cu-based catalysts for selective propane dehydrogenation to propylene assisted by high-throughput computations. *Journal of Catalysis* **2024**, *438*. DOI: 10.1016/j.jcat.2024.115718.

[74] Wang, X.; Zhao, H.; Ma, Y.; Wang, L.; Li, Y.; Chi, L. Discovery of promising Cu-based catalysts for selective propane dehydrogenation to propylene assisted by high-throughput computations. *Journal of Catalysis* **2024**, *438*. DOI: 10.1016/j.jcat.2024.115718.

[75] Sun, X.; Han, P.; Li, B.; Zhao, Z. Tunable Catalytic Performance of Single Pt Atom on Doped Graphene in Direct Dehydrogenation of Propane by Rational Doping: A Density Functional Theory Study. *The Journal of Physical Chemistry C* **2018**, *122* (3), 1570-1576. DOI: 10.1021/acs.jpcc.7b09736.

[76] Montemore, M. M.; Medlin, J. W. Site-Specific Scaling Relations for Hydrocarbon Adsorption on Hexagonal Transition Metal Surfaces. *The Journal of Physical Chemistry C* **2013**, *117* (39), 20078-20088. DOI: 10.1021/jp4076405.

[77] Kong, N.; Fan, X.; Liu, F.; Wang, L.; Lin, H.; Li, Y.; Lee, S.-T. Single Vanadium Atoms Anchored on Graphitic Carbon Nitride as a High-Performance Catalyst for Non-oxidative Propane Dehydrogenation. *ACS Nano* **2020**, *14* (5), 5772-5779. DOI: 10.1021/acsnano.0c00659.

[78] Hou, W.; Lin, K.; Zhang, X.; Xu, B.; Wang, Y.; Lu, X.; Gao, Y.; Ma, R.; Fu, Y.; Zhu, W. Highly stable and selective Pt/TS-1 catalysts for the efficient nonoxidative dehydrogenation of propane. *Chemical Engineering Journal* **2023**, *474*. DOI: 10.1016/j.cej.2023.145648.

[79] Chen, T.; Zhao, S.; Lin, J.; Chong, Y.; Li, Y.; Zhao, Y.; Chen, G.; Qiu, Y. Theoretical and experimental study on the dehydrogenation of propane by oxygen vacancy caused by γ-Al2O3 with the assistance of S. *Surfaces and Interfaces* **2023**, *42*. DOI: 10.1016/j.surfin.2023.103399.

[80] Wu, R.; Chen, B.; Liu, N.; Dai, C.; Xu, R.; Yu, G.; Wang, N.; Xu, Y.; Han, H. NiCrOx@silicalite-1 with Advanced CO2Utilization in Oxidative Dehydrogenation of Propane: Insights into Bifunctional Catalysis and Reaction Efficiency. *ACS Sustainable Chemistry & Engineering* **2025**, *13* (23), 8644-8659. DOI: 10.1021/acssuschemeng.5c02033.